The African dust and smoke layer over the tropical Atlantic during the spring season 2013: Ship-based lidar observations from Guadeloupe to Cape Verde.

Von der Fakultät für Physik und Geowissenschaften
der Universität Leipzig
eingereichte

Masterarbeit

zur Erlangung des akademischen Grades

Master of Science
M. Sc.

vorgelegt von

Franziska Rittmeister, B. Sc.
geboren am 05. Juli 1989 in Erfurt
Matrikelnummer: 3172494

Gutachter:	Jun.–Prof. Dr. Bernhard Pospichal,
	Institut für Meteorologie, Universität Leipzig
Zweitgutachter:	Dr. Albert Ansmann,
	Leibniz–Institut für Troposphärenforschung

Leipzig, den 22. Juli 2015

Contents

Chapter 1

Introduction

Mineral Dust is an omnipresent element in the Earth's atmosphere. The uplift and transportation of Saharan dust is the most important example of long distant distribution of particulate matter. Releasing $700\,\mathrm{Tg\,yr^{-1}}$ [*Laurent et al.*, 2008] the Saharan desert is the world's largest mineral dust source. From there it is spread all over the globe, across the Mediterranean Sea towards Europe and Western Asia, and across the tropical North Atlantic Ocean as far as the Caribbean and South America. In the latter case, mineral dust is transported within a warm, dry, stable, and well-separated Saharan air layer (SAL, *Prospero and Carlson* [1972]). Hence, it has not only regional but also global complex effects on our climate system which can be caused directly by absorption and scattering of solar radiation, absorption, scattering and emission of terrestrial radiation, and change of albedo (see e.g. *Balkanski et al.* [2007]) and indirectly by interaction with clouds, serving as IN or CCN, and fertilization e.g. of the Atlantic Ocean [*Jickells et al.*, 2005] and Amazon region [*Koren et al.*, 2006; *Ansmann et al.*, 2009]. However, during transportation mineral dust particles will ineluctably react with other atmospheric components which effects not only the mineral dusts composition but in case of e.g. heterogeneous reactions with trace gases the chemical balance of the atmosphere [*Bauer et al.*, 2004]. All in all, many of the direct and indirect effects are not understood to the whole extent and as a consequence not well represented in atmospheric prediction models. Mineral dust radiative forcing, for example, is estimated from a slightly negative effect of -0.5 $\mathrm{W\,m^{-2}}$ to a slightly positive effect of 0.5 $\mathrm{W\,m^{-2}}$ [*IPCC*, 2007]. The radiative forcing magnitude and sign are depending on the dust optical properties, its spacial distribution and the reflectance of the underlying surface. Therefore, the investigation of its optical properties is crucial for the understanding of its effects on global radiation balance and consequential effects on climate. Also, vertically resolved observations of those properties are crucial to adequately describe dust layers in atmospheric and aerosol transport models. The latter is required to validate dust transport models [*Heinold et al.*, 2011]. It is known that the physical and chemical properties of dust particles change during their transport due to deposition of larger particles and chemical reactions ('dust aging') [*Prather et al.*, 2008; *Usher et al.*, 2003]. Therefore, it is essential to characterize mineral dust aerosol particles not only in its source region, but also after some time of traveling. Although the general

features of dust over the ocean are known, questions remain regarding the vertical exchange and processing of the dust and the details of the vertical structures of dust layers and the characteristics of each layer [*Jung et al.*, 2013].

In the framework of the Saharan Mineral Dust Experiment (SAMUM) dust optical properties and dust transport have been measured with lidar. Field campaigns [*Tesche et al.*, 2009b, 2011] were conducted near the Saharan dust source (SAMUM–1 in May–June 2006, southern Morocco) and 570 km off the coast of Western Africa (SAMUM–2a in Jan–Feb 2008 and SAMUM–2b in May–Jun 2008, Cape Verde) to derive optical properties near the source and after a short term travel. While during summer 3–5 km deep pure dust layers passed Cape Verde, in winter rather shallow layers of mineral dust from the Sahara and biomass–burning smoke from southern West Africa were observed in the lowermost 1.5 km crossing the Atlantic [*Tesche et al.*, 2011]. During the summer season no significant variation of the intensive optical parameters such as the lidar ratio, Ångström exponent and depolarization ratios could be observed within pure dust layers at both sites in Morocco and Cape Verde. Thus, no significant changes in the particle microphysics could be found during the first days of transport. More details on the Saharan air layer are given in Sect. 2.

In this work, lidar data measured during the research vessel (RV) Meteor cruise in April–May 2013 from the Caribbean to the west coast of Africa are analyzed to characterize the Saharan air layer along the transport route from Cape Verde towards the Caribbean. The cruise was performed in the framework of the Saharan Aerosol Long-range Transport and Aerosol-Cloud-Interaction Experiment (SALTRACE) project which focused on the long–range transport of Saharan dust on the tropical Atlantic [*Ansmann et al.*, 2014]. The optical properties of pure dust, as well as of mixtures of dust, biomass-burning smoke, and marine particles could be determined at several cruise locations. Vertical profiles of four case studies are presented and intensively discussed. Moreover, the one-step POLIPHON method [*Tesche et al.*, 2009b; *Mamouri and Ansmann*, 2014] was applied for the separation of dust and smoke in order to compute dust mass concentration profiles for these cases. Those results are compared to mass concentrations derived by several models to validate their parametrization. The overall goal of the Meteor cruise was to investigate mineral dust optical properties and potential changes during long-range transport.

The thesis is organized as follows. It begins with a brief description of the SAL and the distinct layer characteristics in chapter 2. The basic lidar features and derived quantities and analyzing methods are given in chapter 3. This chapter also presents the POLIPHON aerosol particle type separation method. Instruments applied aboard the RV Meteor, in particular the Polly^{XT} lidar, are presented in chapter 4. Chapter 5 contains basic information about distinct aerosol transport models. The ship-based lidar observations are discussed in chapter 6. This chapter contains a measurement overview, case studies, a statistical analysis, and model comparison to the lidar findings. Chapter 7 concludes with a summary and outlook.

Chapter 2

The Saharan air layer (SAL)

Mineral dust particles mainly consists of silicates and carbonates [*Kandler et al.*, 2009]. They are compositionally heterogeneous and a typical dust composition does not exist [*Scheuvens and Kandler*, 2014; *Kandler et al.*, 2011]. Due to their non–spherical shape dust particles cause a relatively high linear depolarization ratio of 14±3% and 39±5% for submicrometer and supermicrometer Saharan dust particles, respectively [*Sakai et al.*, 2010]. The depolarization ratio is explained in the next chapter.

Saharan dust particles can be emitted naturally by three distinct processes [*Shao*, 2001, 2008]: direct aerodynamic lifting, ejection of dust aerosol particles from soil aggregates by impacting saltating particles, and ejection of dust from soil aggregates that are participating in saltation. Due to turbulence, convection and wind, the aerosol particles are uplifted in the atmosphere. There it forms the Saharan air layer (SAL), an elevated layer of Saharan air and mineral dust extending up to 500 hPa [*Dunion and Velden*, 2004] (see Fig. 2.1 left) during summer months.

The SAL is warm (potential temperature of $\sim$313–317 K), dry (mixing ratios of $\sim$2–4 g kg^{-1}), and well-mixed [*Jung et al.*, 2013]. A major part of the suspended Saharan mineral dust is exported towards the northern tropical Atlantic by the influence of the easterly trade wind and African easterly waves [*Prospero and Carlson*, 1972; *Romero et al.*, 1999] where it can be observed during the late spring through early fall with maximum dust concentrations at $\sim$5°N in winter and $\sim$20°N in summer [*Moulin et al.*, 1997]. Offshore the SAL is undercut by cool, moist marine air (Fig. 2.1 middle). The marine boundary layer (MBL) generally deepens offshore. Primary marine particles produced directly from the ocean surface initiated by wind shear are composed of sea salt and organic matter. They are known as efficient cloud condensation nuclei (CCN) due to their size and hygroscopicity. At this state the SAL retains its characteristics of warm, stable air near its base ($\sim$850 hPa in summer), and dryness and dustiness throughout its depth as it is carried as far as the western Caribbean Sea ($\sim$7000 km from the African coast) [*Dunion and Velden*, 2004].

A study presented by [*Jung et al.*, 2013] shows vertical profiles of three dust-loaded layers with distinct aerosol and thermodynamic characteristics near Barbados (Fig. 2.1 right). Following information on those layers are taken from this work if not otherwise quoted. Below
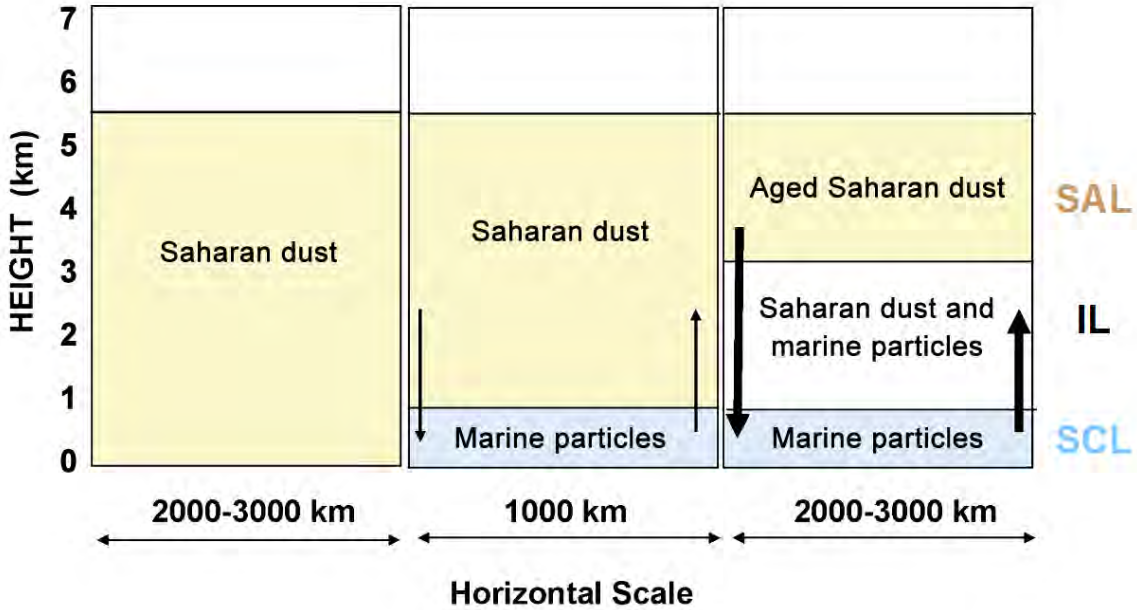
Figure 2.1: Vertical distribution of Saharan dust during the summer half year over the African continent (left), over the tropical Atlantic (center), and over the tropical Atlantic during transport towards the Caribbean (right). Arrows in this sketch indicate mixing processes between the distinct aerosol layers.

the SAL, an intermediate layer (IL) and a sub cloud layer (SCL) could be distinguished with decreasing aerosol particle concentrations of 300–$700\,\mathrm{cm}^{-3}$ observed in the SAL and 200–$400\,\mathrm{cm}^{-3}$ in the SCL. While both the SAL and SCL could be characterized as well-mixed layers, the IL showed high thermodynamic and aerosol variability due to temporal cumulus formation. Furthermore, the layers up to $1700\,\mathrm{m}$ seem to be moistened by surface fluxes during long-range transport, while the SAL subsided $125\,\mathrm{m\,d}^{-1}$ and cooled down $0.5^\circ\,\mathrm{C\,d}^{-1}$. Similar values of sinking 85–$175\,\mathrm{m\,d}^{-1}$ and cooling $0.7^\circ\,\mathrm{C\,d}^{-1}$ are indicated by *Carlson and Prospero* [1972]. The low cooling rate can be explained by the intense initial warming over North Africa and the steady absorption of solar radiation by the suspended mineral dust particles. Former researches point out that the SAL strongly affects the activity of tropical cyclones (TC). Its dry, stable air and strong easterly wind shear weakens the TC updrafts [*Dunion and Velden*, 2004] whereas *Chen* [1985] shows that along the SAL boundaries TC activity can be rapidly enhanced.

During the winter half year (Nov–Apr), which is the biomass–burning season (dry season) in Central Africa, smoke particles get mixed into the SAL leading to complex aerosol conditions. Figure 2.2 shows the ITCZ (Inter–Tropical Convergence Zone) shift and the active fires areas south of the SAL source region using the example of the SAMUM campaign. In summer, the ITCZ shifts northward and the maximum of fire activity occurs in southern parts of Africa. Layers of pure mineral dust are then transported westwards from the west coast of North Africa over the Atlantic Ocean. However, during winter the ITCZ retreats south and
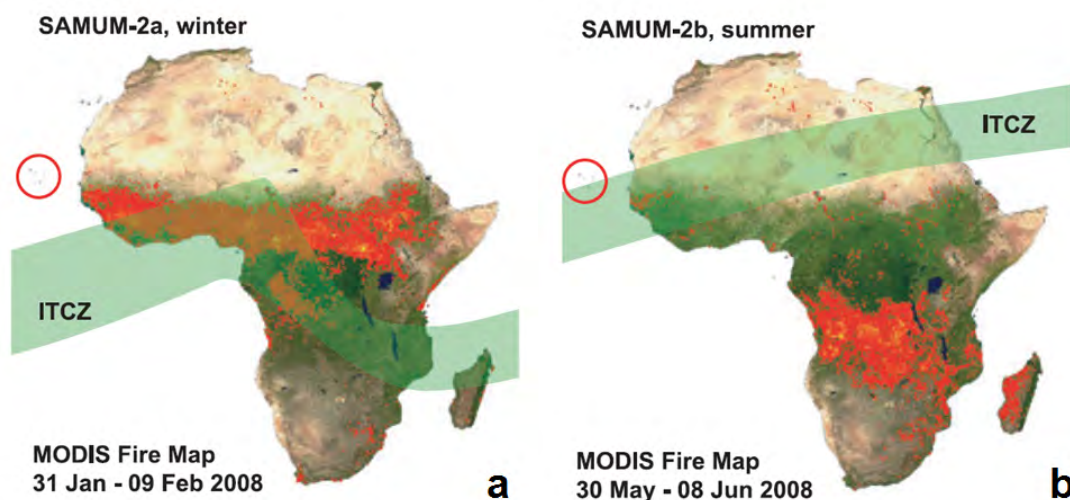
Figure 2.2: ITCZ position (green shaded) in winter (**a**) and summer (**b**) during SAMUM–2a and SAMUM–2b, respectively, underlaid with MODIS firemaps [*Tesche et al.*, 2011].

a band of biomass–burning activity in equatorial Africa stretches up to $15°N$, so that the mineral dust aerosol layer gets contaminated by aerosols from those burning activities (see e.g. *Prospero and Carlson* [1972]). *Tesche et al.* [2011] shows that the aerosol layer maximum height is on average lower in winter at 3–6 km compared to the summer average aerosol layer top height at 5–6 km. Also rather shallow aerosol layers of 1–3 km depth only were observed during the winter season. The boundary layer height is <3 km and 4-6 km over the African desert in winter and summer, respectively.

Still questions remain regarding the vertical transport and processing of the dust and the details of the vertical structures of dust layers and the characteristics of each layer. Mineral dust, marine particles, and smoke have been specified in terms of their optical properties during the SAMUM campaigns near the source region and after short–term transport. Table 2.1 shows the overall findings. These data are used for comparison with findings obtained during the RV Meteor cruise (chapter 6).

Table 2.1: Summary of the SAMUM campaign findings in terms of mean $500\,\text{nm}$ AOT, average aerosol layer depth, and extensive (particle backscatter and extinction coefficient, β^p and α^p) and intensive parameters (lidar ratio S, Ångström exponent $\mathring{a}^\alpha$ and $\mathring{a}^\beta$, and particle depolarizations ratios δ^p) at various wavelengths from 355–1064 nm. Values for SAMUM–1 are taken from *Freudenthaler et al.* [2009] (particle depolarization ratios) and *Tesche et al.* [2009a] (lidar ratios and Ångström exponents). SAMUM–2 values are taken from *Tesche et al.* [2011] and *Groß et al.* [2011]. By analogy with the descriptions β^p, α^p, S, $\mathring{a}^\alpha$, $\mathring{a}^\beta$, and δ^p, we will use the notations β_{aer}, α_{aer}, S, $\mathring{a}_\alpha$, $\mathring{a}_\beta$, and δ_{aer} in this work from now on.

Campaign	SAMUM-1 Morocco May/June 2006		SAMUM-2a Cape Verde January/February 2008			SAMUM-2b Cape Verde May/June 2008
Mean 500-nm AOT	0.31 ± 0.17		0.35 ± 0.18			0.40 ± 0.20
Aerosol layer top height (km)	3.8 ± 0.8		3.5 ± 1.2			4.4 ± 0.7
Mean values between 2 and 4 km height asl						
β^{p}_{355} ($\text{M m}^{-1}\,\text{sr}^{-1}$)	1.7 ± 0.2		1.4 ± 0.2			1.4 ± 0.2
β^{p}_{532} ($\text{M m}^{-1}\,\text{sr}^{-1}$)	1.5 ± 0.1		0.8 ± 0.1			1.4 ± 0.1
β^{p}_{1064} ($\text{M m}^{-1}\,\text{sr}^{-1}$)	1.4 ± 0.1		0.5 ± 0.1			1.1 ± 0.1
α^{p}_{355} (M m^{-1})	97 ± 23		66 ± 6			83 ± 6
α^{p}_{532} (M m^{-1})	97 ± 23		48 ± 5			79 ± 4

	Specific findings for different aerosol types					
Aerosol type	Dust	Maritime	Dust+smoke	Dust	Smoke	Dust
Mean layer depth (km)	3.8 ± 0.8	0.4 ± 0.1	3.8 ± 0.8	1.0 ± 0.4	–	4.1 ± 0.7
S_{355} (sr)	53 ± 7	17	67 ± 14	58	87 ± 17	53 ± 10
S_{532} (sr)	55 ± 7	18	67 ± 12	61	79 ± 17	54 ± 10
S_{1064} (sr)	55 ± 13	–	–	–	–	–
$\mathring{a}^{\alpha}_{355/532}$	0.06 ± 0.21	–	0.67 ± 0.38	–	1.15 ± 0.28	0.22 ± 0.27
$\mathring{a}^{\beta}_{355/532}$	0.19 ± 0.20	–	0.71 ± 0.28	–	0.90 ± 0.26	0.16 ± 0.45
$\mathring{a}^{\beta}_{532/1064}$	0.28 ± 0.16	–	0.67 ± 0.27	–	1.06 ± 0.65	0.45 ± 0.16
δ^{p}_{355}	0.26 ± 0.06	0.03	0.16 ± 0.04	0.25	–	–
δ^{p}_{532}	0.31 ± 0.03	0.03	0.16 ± 0.03	0.30	0.05 ± 0.02	0.31 ± 0.10
δ^{p}_{710}	0.28 ± 0.05[1]	–	0.18 ± 0.03	0.36	–	0.37 ± 0.07

Chapter 3

Lidar setup and function

3.1 Atmospheric light scattering

The two major processes of light scattering in the atmosphere are Rayleigh scattering and Mie scattering. Both correspond to the Lorenz–Mie theory for spherical particles. The Rayleigh scattering approximation denotes elastic scattering by particles much smaller than the wavelength of the regarded radiation. In this case the scattering efficiency is proportional to λ^{-4} which means incident light at larger wavelengths is less scattered by the small air molecules. Furthermore, the intensity of Rayleigh scattered radiation is identical in the forward and reverse direction.

For particles with larger size, the Mie scattering model introduced by [*Mie*, 1908] can be used. It is less dependent on the wavelength and the intensity of Mie scattered radiation is larger in the forward direction than in the reverse direction. It yields, the larger the particle dimension, the more light is scattered in the forward direction. If the particle dimensions are not much larger than the wavelength of the scattered radiation the Mie theory can be applied as an approximation to non-spherical particles as well [*Wandinger et al.*, 2002; *Müller et al.*, 2007b; *Böckmann*, 2001]. In contrast, due to their strongly irregular shape the classical Mie theory it is not applicable in the case of desert dust particles. This poses large difficulties to radiative transfer modeling. A spheroidal particle shape is therefore often assumed for mineral dust particles *Dubovik et al.* [2006].

Both Mie and Rayleigh scattering are elastic processes, which means conservation of energy and no alteration in the wavelength of the light. On the contrary Raman scattering describes light scattering processes which induce a wavelength shift due to inelastic scattering. When light hits an atmospheric molecule its electrons can absorb some of the photon's energy (Stokes Raman scattering) or add some energy (anti-Stokes Raman scattering) to the initial photon energy. In this case the transferred energy leads to changes of the molecules vibrational or rotational state and a frequency shift of the backscattered light. The frequency shift, and hence the wavelength shift, is characteristic for the scattering molecule. Figure 3.1 shows the atmospheric Raman backscatter spectrum for a stimulation wavelength of 355 nm. Thus, it
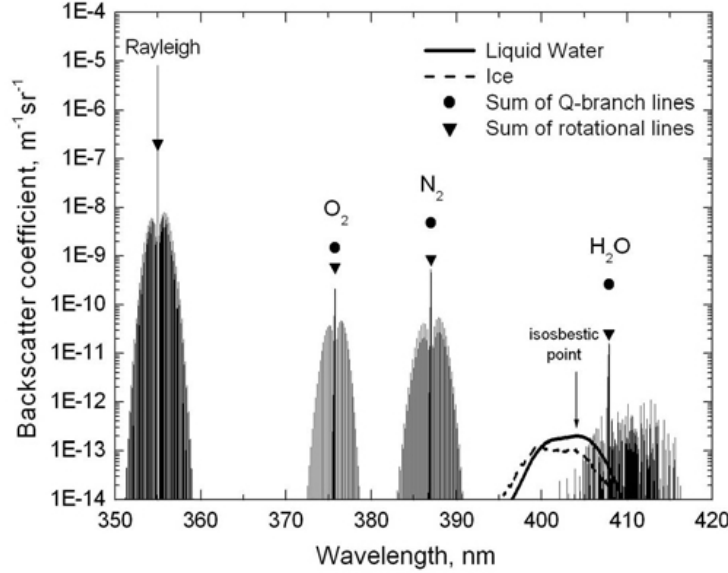
Figure 3.1: Atmospheric Raman spectrum for a stimulation wavelength of 355 nm, normal pressure, a temperature of 300 K, an N_2 and O_2 content of 0.781 and 0.209, respectively, and a water-vapor mixing ratio of 10 g/kg. The curves for liquid water and ice are arbitrarily scaled [*Wandinger*, 2005].

appears that a spectrally resolved analysis of backscattered radiation allows the measurement of various atmospheric species. Raman scattering active gases in the atmosphere of known number concentration (oxygen, nitrogen) can be used as reference values in this process.

3.2   General Lidar setup

Lidar systems ('Light Detection And Ranging') are measurement instruments within the field of active remote sensing. Basically, such consist of an emitter and receiver unit as shown in Fig. 3.2. A laser belonging to the emitter unit generates a monochromatic and coherent laser pulse from 250 nm to 11 μm which is sent into the atmosphere. Caused by various extinction processes in different height levels, the laser light can be absorbed or scattered by molecules and atmospheric particles (e.g. aerosols, clouds, precipitation etc.). The backscattered light of vertically pointing lidar gives information about the state and composition of the air masses above the measurement instrument. The backscattered photons are collected by a telescope (mostly a mirror telescope) and transferred to optical detectors such as photomultiplier tubes (PMT) or photo diodes which are able to count discrete photons.

The signal can be separated into wavelengths and states of polarization using interference and polarization filters depending on system usage. Detectors convert radiation into an electronic signal with high temporal resolution. Thus, the signal strength can be stored in dependence
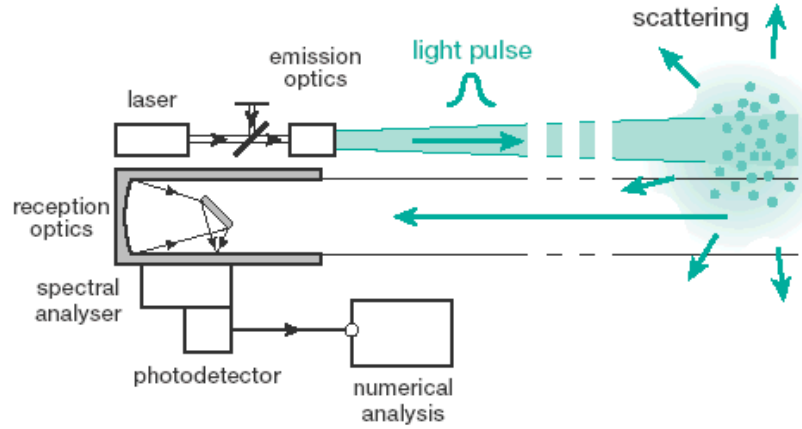
Figure 3.2: Lidar system setup [*http://www.smsc.cnes.fr/*].

of the time passing between pulse emission and signal detection. Gained lidar signals are averaged over values of few seconds or minutes to reduce the amount of recorded and stored data.

The more bundled (or collimated) the emitted laser beam the smaller the telescope field of view can be chosen. This is essential to reduce confounding factors such as sky background radiation and multiply scattered photons. Telescopes with an area of 0.1 m to several meters are applied. Construction and arrangement of the lidar receiver unit determine from which height range backscattered photons can be used for atmospheric studies. The lidar geometrical properties are considered in the overlap function which describes the overlap between the laser beam and the receiver field of view (RFOV). So–called near–range (N/R) and far–range lidar measurements are distinguished. The N/R covers the height range from about 50–100 m to several kilometers, whereas the far–range telescope is able to properly collect photons from a few hundred meters up to stratospheric heights.

3.3 Lidar principle and equation

Lidar setups are active remote sensing measurement instruments. A monochromatic and coherent laser pulse at power P_0 is sent into the atmosphere. The receiver unit detects the backscattered signal P. The range R of the scattering height level and time t between pulse emission and signal detection are linked as follows with known light speed c:

$$R = \frac{ct}{2} \tag{3.1}$$

The factor $\frac{1}{2}$ in Eq. 3.1 indicates the double covered way through the atmosphere of the emitted pulse to the backscattering air mass and back to the instrument. The gained signal

can be described by the lidar equation [*Wandinger*, 2005]:

$$P(R,\lambda) = \underbrace{P_0(\lambda)\frac{c\tau(\lambda)}{2}\eta(\lambda)A_{\text{Tel}}}_{\text{I}}\,\underbrace{\frac{O(R)}{R^2}}_{\text{II}}\,\underbrace{\beta(R,\lambda)}_{\text{III}}\,\underbrace{\exp\left[-2\int_0^R \alpha(r,\lambda)\,\mathrm{d}r\right]}_{\text{IV}}. \qquad (3.2)$$

It contains following parameters:

λ	[m]	the detected wavelength,
R	[m]	the distance from the lidar receiver,
$P_0(\lambda)$	[W sr^{-1}]	the emitted pulse power,
$P(R,\lambda)$	[W sr^{-1}]	the detected power,
$\tau(\lambda)$	[s]	the temporal pulse length,
c	[m s^{-1}]	the velocity of light,
$\eta(\lambda)$		the system efficiency,
A_{Tel}	[m^2]	the receiver telescope area,
$O(R)$		the overlap function,
$\beta(R,\lambda)$	[m^{-1}sr^{-1}]	the backscatter coefficient, and
$\alpha(R,\lambda)$	[m^{-1}]	the extinction coefficient.

Term I of the lidar equation 3.2 shows the system factor which includes instrument specific properties. To these belong the power of a single emitted laser pulse $P_0(\lambda)$ of wavelength λ, the temporal pulse length $\tau(\lambda)$, the transmission efficiency $\eta(\lambda)$ and the area A_{Tel} of the receiver telescope in which the backscattered signal is detected.

The second term II denotes the range–dependent geometrical measurement properties and includes the overlap function $O(R)$ of laser beam and receiver field of view. Moreover, it depicts the squared decrease in signal power with distance between instrument and scattering volume. $O(R)$ is 0 at the measurement instrument and 1 if the laser beam can be completely depicted by the detector.

The lidar equation also contains the backscatter coefficient $\beta(R,\lambda)$ (term III) which influences the detected signal power most amongst all mentioned atmospheric parameters. It describes how much radiation is scattered at an angle of 180°, and thus directly into the direction of the receiver unit. Laser pulse photons can be scattered by molecules (index mol) as well as particles (index aer) in the atmosphere. Thus, the backscatter coefficient consists of molecular and particle part:

$$\beta(R,\lambda) = \beta_{\text{mol}}(R,\lambda) + \beta_{\text{aer}}(R,\lambda). \qquad (3.3)$$

Finally, the transmission term IV which results from the Lambert-Beert-Bougert law is included in the lidar Eq. 3.2. It contains information about the part of attenuated radiation and can assume values between 0 (radiation is attenuated completely) and 1 (no extinction at all). The extinction coefficient $\alpha(R,\lambda)$ is integrated over range from the lidar ($R=0$) to the height R. The factor 2 again indicates the two–way photon travel path. Similar to Eq.

3.3 the extinction coefficient can be written as:

$$\alpha(R, \lambda) = \alpha_{\text{mol,sca}}(R, \lambda) + \alpha_{\text{mol,abs}}(R, \lambda) + \alpha_{\text{aer,sca}}(R, \lambda) + \alpha_{\text{aer,abs}}(R, \lambda). \qquad (3.4)$$

Extinction is divided into scattering (index sca) and absorption (index abs). Lidar equation 3.2 holds for elastic backscattering by particles and molecules and is the basic equation for the retrieval of the particle backscatter coefficient $\beta_{\text{aer}}(R, \lambda_0)$ by the so–colled Klett method (Sect. 3.4).

3.4 Klett method

For atmospheric studies we can derive the particle backscatter coefficient $\beta_{\text{aer}}(R, \lambda_0$ by means of the Fernald-Klett-Method [*Fernald*, 1984; *Klett*, 1981]:

$$\beta_{\text{aer}}(R, \lambda_0) = \frac{A(R_0, R, \lambda_0)}{B(R_0, \lambda_0) - 2S_{\text{aer}}(\lambda_0) \int_{R_0}^{R} A(R_0, r, \lambda_0)\, \mathrm{d}r} - \beta_{\text{mol}}(R, \lambda_0), \qquad (3.5)$$

with

$$A(R_0, x, \lambda_0) = x^2 P(x, \lambda_0) \exp\left[-2(S_{\text{aer}}(\lambda_0) - S_{\text{mol}}) \int_{R_0}^{x} \beta_{\text{mol}}(r, \lambda_0)\, \mathrm{d}r\right] \qquad (3.6)$$

and

$$B(R_0, \lambda_0) = \frac{R_0{}^2 P(R_0, \lambda_0)}{\beta_{\text{aer}}(R_0, \lambda_0) + \beta_{\text{mol}}(R_0, \lambda_0)}. \qquad (3.7)$$

Here, the reference height R_0 is introduced and the backscatter coefficient $\beta_{\text{par}}(R_0, \lambda_0)$ for this reference height has to be assumed. The reference height is set into a height layer in which particle scattering is very small compared to Rayleigh backscattering (which is known) to keep the overall uncertainty in the reference backscatter assumption small. Furthermore, to solve Eq. 3.5 the lidar ratio $S_{\text{aer}}(\lambda_0)$ defined on the ratio of particle extinction to backscatter coefficients (Eq. 3.11) has to be assumed. Usually, a characteristic lidar ratio is assumed, e.g. 50 sr for urban haze, 20 sr for pure marine particles, or 50–60 sr for desert dust.

3.5 Raman–lidar method

For the independent determination of the particle extinction and backscatter coefficients the Raman lidar method is applied. Here, the inelastically backscattered lidar signal $P(R, \lambda_{\text{Ra}})$ caused by molecular Raman scattering is detected in addition to the elastically scattered component $P(R, \lambda_0)$. Due to the transfer of energy during inelastic scattering (see Sect. 3.3) the initial wavelength λ_0 is altered to the Raman wavelength λ_{Ra}. The detected power at the Raman wavelength can be described as follows [*Wandinger*, 2005; *Ansmann et al.*, 1990]:

$$P(R, \lambda_{\text{Ra}}) = \underbrace{P_0(\lambda_0) K_s(\lambda_{\text{Ra}})}_{\text{I}_{\text{Ra}}} \underbrace{\frac{O(R)}{R^2}}_{\text{II}_{\text{Ra}}} \underbrace{\beta_{\text{Ra}}(R, \lambda_{\text{Ra}})}_{\text{III}_{\text{Ra}}} \underbrace{\exp\left[-\int_0^R \alpha(r, \lambda_0) + \alpha(r, \lambda_{\text{Ra}}) \mathrm{d}r\right]}_{\text{IV}_{\text{Ra}}}. \qquad (3.8)$$

$P_0(\lambda_0)$ depicts the emitted laser power. According to Eq. 3.2 the first term now contains a λ_{Ra} related system factor. The backscatter coefficient β_{Ra} is measured at the Raman wavelenght λ_{Ra} as well. Here, the transmission term $\mathrm{IV}_{\mathrm{Ra}}$ consists of an elastic part $\alpha(R, \lambda_0)$ for the way up at wavelength λ_0 and for the way back at the Raman–shifted wavelength λ_{Ra} ($\alpha(R, \lambda_{\mathrm{Ra}})$).

Using the Raman method, profiles of both extinction and backscatter coefficients can be derived directly and independently by measurements of the elastically signal $P(R, \lambda_0)$ (see equation 3.2) and the Raman signal $P(R, \lambda_{\mathrm{Ra}})$. The extinction coefficient can be determined as follows [*Ansmann et al.*, 1990]:

$$\alpha_{\mathrm{aer}}(R, \lambda_0) = \frac{\frac{\mathrm{d}}{\mathrm{d}R}\left[\ln \frac{N_{\mathrm{Ra}}(R)}{R^2 P_{\mathrm{Ra}}(R)}\right] - \alpha_{\mathrm{mol}}(R, \lambda_0) - \alpha_{\mathrm{mol}}(R, \lambda_{\mathrm{Ra}})}{1 + (\frac{\lambda_0}{\lambda_{\mathrm{Ra}}})^{\mathring{a}_\alpha}}, \qquad (3.9)$$

with the molecular particle number density N_{Ra} of the regarded gas. Oxygen and nitrogen are suitable for Raman method implementation because their particle number density profiles are sufficiently well known. They can be calculated by temperature and preassure profiles derived by nearby soundings or by means of atmospheric model data. The Ångström exponent $\mathring{a}_\alpha$ describes the dependency of the extinction coefficient on the wavelength (see Eq. 3.12a). The use of these two independently measured signals, elastic and Raman signals, leads to profiles of the particle backscatter coefficient [*Ansmann et al.*, 1992]:

$$\begin{aligned}
\beta_{\mathrm{aer}}(R, \lambda_0) &= [\beta_{\mathrm{aer}}(R_0, \lambda_0) + \beta_{\mathrm{mol}}(R_0, \lambda_0)] \\
&\times \frac{P(R_0, \lambda_{\mathrm{Ra}})P(R, \lambda_0)}{P(R_0, \lambda_0)P(R, \lambda_{\mathrm{Ra}})} \frac{N_{\mathrm{Ra}}(R)}{N_{\mathrm{Ra}}(R_0)} \\
&\times \frac{\exp\{-\int_{R_0}^{R}[\alpha_{\mathrm{aer}}(r, \lambda_{\mathrm{Ra}}) + \alpha_{\mathrm{mol}}(r, \lambda_{\mathrm{Ra}})]\,\mathrm{d}r\}}{\exp\{-\int_{R_0}^{R}[\alpha_{\mathrm{aer}}(r, \lambda_0) + \alpha_{\mathrm{mol}}(r, \lambda_0)]\,\mathrm{d}r\}} \\
&- \beta_{\mathrm{mol}}(R, \lambda_0).
\end{aligned} \qquad (3.10)$$

R_0 is the reference height in which pure molecule signal dominates. Again, the reference backscatter coefficient $\beta_{\mathrm{par}}(R_0, \lambda_0)$ must be assumed *a priori*. A lidar ratio estimate is not needed here.

3.6   Basic aerosol particle optical properties

From the basic backscatter and extinction coefficients several intensive particle parameters can be determined. The relationship between the backscatter and extinction coefficient is expressed by the lidar ratio (extinction-to-backscatter ratios) for atmospheric particles (Eq.

3.11a) and molecules (Eq. 3.11b):

$$S_{\text{aer}}(\lambda, R) = \frac{\alpha_{\text{aer}}(\lambda, R)}{\beta_{\text{aer}}(\lambda, R)} \tag{3.11a}$$

$$S_{\text{mol}}(\lambda, R) = \frac{\alpha_{\text{mol}}(\lambda, R)}{\beta_{\text{mol}}(\lambda, R)}. \tag{3.11b}$$

The Ångström exponent $\mathring{a}$ expresses the dependency of the optical aerosol properties on the wavelength [*Ångström*, 1964; *Ansmann and Müller*, 2005]. It can be determined by the backscatter coefficient α or extinction coefficient β, measured at two wavelengths λ_0 and λ_1 as follows:

$$\mathring{a}_\alpha(R) = -\frac{\ln\left(\frac{\alpha_{\text{aer}}(\lambda_1)}{\alpha_{\text{aer}}(\lambda_0)}\right)}{\ln\left(\frac{\lambda_1}{\lambda_0}\right)} \tag{3.12a}$$

$$\mathring{a}_\beta(R) = -\frac{\ln\left(\frac{\beta_{\text{aer}}(\lambda_1)}{\beta_{\text{aer}}(\lambda_0)}\right)}{\ln\left(\frac{\lambda_1}{\lambda_0}\right)}. \tag{3.12b}$$

Since the Ångström exponent is inversely proportional to the average particle size, information about the observed particle sizes can be gathered from it. That yields, the smaller the particles the bigger the Ångström exponent. Therefore, if the Ångström exponent is invariant, it indicates constant aerosol properties. It can also be derived from sun–photometer measurements of the aerosol optical depth (AOD) or optical thickness (AOT) τ:

$$\mathring{a}_\tau(R) = -\frac{\ln\left(\frac{\tau(\lambda_1)}{\tau(\lambda_0)}\right)}{\ln\left(\frac{\lambda_1}{\lambda_0}\right)} \tag{3.13}$$

This parameter from photometer measurement will be used in the data analysis later on. The AOT is dimensionless and describes the degree to which aerosols prevent the transmission of light. It is defined as the integrated extinction coefficient over a vertical column of unit cross section and can therefore be calculated by the use of lidar data:

$$\tau(\lambda) = \int_{z_0}^{z} \alpha(\lambda)\, \mathrm{d}z \tag{3.14}$$

3.7   Polarization–lidar method

Due to the particle geometrical properties the state of polarization of the emitted light can be altered while scattering processes. Therefore, information about the sphericity of the atmospheric particles can be gathered from the state of polarization of the backscattered light. In addition to the unpolarized light (index $\parallel$) the backscattered light component which is perpendicularly polarized (index $\perp$) with respect to the polarization plane of the unpolarized

light is detected to derive the volume depolarization ratio and the particle depolarization ratio, respectively:

$$P^{\parallel}(\lambda, R) = \frac{1}{R^2} P_0(\lambda, R) O(R) K_{\mathrm{s}}{}^{\parallel}(\lambda) \beta^{\parallel}(\lambda, R) \exp\left[-2\int_0^R \alpha(r, \lambda_0) \mathrm{d}r\right] \qquad (3.15\mathrm{a})$$

$$P^{\perp}(\lambda, R) = \frac{1}{R^2} P_0(\lambda, R) O(R) K_{\mathrm{s}}{}^{\perp}(\lambda) \beta^{\perp}(\lambda, R) \exp\left[-2\int_0^R \alpha(r, \lambda_0) \mathrm{d}r\right] \qquad (3.15\mathrm{b})$$

where $\beta^{\perp}$ is the cross–polarized and $\beta^{\parallel}$ the parallel-polarized backscatter coefficient. As in equation 3.3 they can be separated into a molecular and aerosol particle part. Since the emitted power P_0 and the transmission term are equal for the parallel and perpendicular polarized light, which is also assumed here for the overlap function $O(R)$ and the system factor K_{s}, the volume depolarization ratio δ_{vol} can be simply written as

$$\delta_{\mathrm{vol}}(\lambda, R) = \frac{P^{\perp}(\lambda, R)}{P^{\parallel}(\lambda, R)} = \frac{\beta^{\perp}(\lambda, R)}{\beta^{\parallel}(\lambda, R)} = \frac{\beta_{\mathrm{mol}}^{\perp}(\lambda, R) + \beta_{\mathrm{aer}}^{\perp}(\lambda, R)}{\beta_{\mathrm{mol}}^{\parallel}(\lambda, R) + \beta_{\mathrm{aer}}^{\parallel}(\lambda, R)}. \qquad (3.16)$$

The separation of the particle depolarization ratio δ_{aer}

$$\delta_{\mathrm{aer}}(\lambda, R) = \frac{\beta_{\mathrm{aer}}^{\perp}(\lambda, R)}{\beta_{\mathrm{aer}}^{\parallel}(\lambda, R)}, \qquad (3.17)$$

and the molecular depolarization ratio δ_{mol}

$$\delta_{\mathrm{mol}}(\lambda, R) = \frac{\beta_{\mathrm{mol}}^{\perp}(\lambda, R)}{\beta_{\mathrm{mol}}^{\parallel}(\lambda, R)} \qquad (3.18)$$

is not a simple task. According to *Tesche et al.* [2009b] the particle depolarization ratio δ_{aer} is obtained from

$$\delta_{\mathrm{aer}}(\lambda, R) = \frac{\beta_{\mathrm{mol}}(\lambda, R)(\delta_{\mathrm{vol}}(\lambda, R) - \delta_{\mathrm{mol}}(\lambda, R)) + \beta_{\mathrm{aer}}(\lambda, R)\delta_{\mathrm{vol}}(\lambda, R)(1 + \delta_{\mathrm{mol}}(\lambda, R))}{\beta_{\mathrm{mol}}(\lambda, R)(\delta_{\mathrm{mol}}(\lambda, R) - \delta_{\mathrm{vol}}(\lambda, R)) + \beta_{\mathrm{aer}}(\lambda, R)(1 + \delta_{\mathrm{mol}}(\lambda, R))}. \qquad (3.19)$$

In the case of spherical particles (solution droplets, cloud droplets), the particle depolarization ratio is close to zero ($\delta_{\mathrm{aer}} \sim 0$) if multiple scattering (in dense clouds) can be neglected. The incident linear polarized light is backscattered without a change of the polarization state. For non-spherical particles such as ice crystals or mineral dust particles, however, the backscattered signal contains a cross–polarized component which results in depolarization ratio in the range of $0.2 < \delta_{\mathrm{aer}} < 0.6$. In the case of Polly$^{\mathrm{XT}}$ (see Sect. 4.2), the parallel–polarized signal component $P^{\parallel}$ is not measured but calculated from the total and cross–polarized signal components.

3.8 Aerosol particle type separation: The POLIPHON method

In the case of mixed aerosol layers, such as layers consisting of mineral dust and biomass–burning aerosol particles, knowledge of the vertical distribution of the individual aerosol types is crucial for an understanding of their impact on climate (e.g. radiation field, cloud processes). The polarization–lidar photometer networking (POLIPHON, *Ansmann et al.* [2011], *Ansmann et al.* [2012]) method is used to separate dust and non-dust aerosol particles in terms of the backscattering, extinction, volume concentration, and mass concentration. The parallel–polarized $\beta_{\mathrm{aer}}^{\parallel}$ and cross–polarized $\beta_{\mathrm{aer}}^{\perp}$ particle backscatter coefficients are assumed to be composed of non-dust (index nd) and dust (index d) particle components

$$\beta_{\mathrm{aer}}^{\parallel} = \beta_{\mathrm{nd}}^{\parallel} + \beta_{\mathrm{d}}^{\parallel}, \tag{3.20a}$$

$$\beta_{\mathrm{aer}}^{\perp} = \beta_{\mathrm{nd}}^{\perp} + \beta_{\mathrm{d}}^{\perp}. \tag{3.20b}$$

Thus, the particle depolarization ratio (see equation 3.17) can be written as

$$\delta_{\mathrm{aer}} = \frac{\beta_{\mathrm{aer}}^{\parallel}}{\beta_{\mathrm{aer}}^{\perp}} = \frac{\beta_{\mathrm{nd}}^{\parallel} + \beta_{\mathrm{d}}^{\parallel}}{\beta_{\mathrm{nd}}^{\perp} + \beta_{\mathrm{d}}^{\perp}}. \tag{3.21}$$

Using the relations $\beta_{\mathrm{nd}} = \beta_{\mathrm{nd}}^{\parallel} + \beta_{\mathrm{nd}}^{\perp}$ and $\beta_{\mathrm{d}} = \beta_{\mathrm{d}}^{\parallel} + \beta_{\mathrm{d}}^{\perp}$, *Tesche et al.* [2009b] shows that the particle depolarization ratio can be transformed to

$$\delta_{\mathrm{aer}} = \frac{\beta_{\mathrm{nd}}\delta_{\mathrm{nd}}(1 + \delta_{\mathrm{d}}) + \beta_{\mathrm{d}}\delta_{\mathrm{d}}(1 + \delta_{\mathrm{nd}})}{\beta_{\mathrm{nd}}(1 + \delta_{d}) + \beta_{\mathrm{d}}(1 + \delta_{\mathrm{nd}})}. \tag{3.22}$$

By substituting β_{nd} by $\beta_{\mathrm{aer}} - \beta_{\mathrm{d}}$ and after further rearranging, the solution for β_{d} is given by

$$\beta_{\mathrm{d}} = \beta_{\mathrm{aer}}\frac{(\delta_{\mathrm{aer}} - \delta_{\mathrm{nd}})(1 + \delta_{\mathrm{d}})}{(\delta_{\mathrm{d}} - \delta_{\mathrm{nd}})(1 + \delta_{\mathrm{aer}})}, \tag{3.23}$$

which is valid for particle depolarization ratios of $\delta_{\mathrm{nd}} \leq \delta_{\mathrm{aer}} \leq \delta_{\mathrm{d}}$. The profile of the non–dust backscatter coefficient is obtained as $\beta_{\mathrm{nd}} = \beta_{\mathrm{aer}} - \beta_{\mathrm{d}}$. For depolarization ratios $\delta_{\mathrm{aer}} \leq \delta_{\mathrm{nd}}$ it yields $\beta_{\mathrm{nd}} = \beta_{\mathrm{aer}}$, and for depolarization ratios $\delta_{\mathrm{aer}} \geq \delta_{\mathrm{d}}$ we set $\beta_{\mathrm{d}} = \beta_{\mathrm{aer}}$.
By means of the dust and non–dust backscatter coefficient profiles and characteristic lidar ratios S the mass concentration profiles for dust and non–dust particles can be calculated as shown by *Ansmann et al.* [2012]:

$$M_{\mathrm{d}} = \rho_{\mathrm{d}}(\nu_{\mathrm{d}}/\tau_{\mathrm{d}})\beta_{\mathrm{d}}S_{\mathrm{d}}, \tag{3.24a}$$

$$M_{\mathrm{nd}} = \rho_{\mathrm{nd}}(\nu_{\mathrm{nd}}/\tau_{\mathrm{nd}})\beta_{\mathrm{nd}}S_{\mathrm{nd}}. \tag{3.24b}$$

ρ_{d} and ρ_{nd} are the particle densities of dust and non–dust particles, respectively. The conversion factors $\nu_{\mathrm{d}}/\tau_{\mathrm{d}}$ and $\nu_{\mathrm{nd}}/\tau_{\mathrm{nd}}$ consist of the column particle volume concentration ν_{d} and ν_{nd}, and the optical thicknesses τ_{d} and τ_{nd} for the respective aerosol types. These conversion

factors are determined from AERONET photometer observations.

In this work, the non–dust particles are considered to be marine particles within the marine boundary layer (MBL, at heights $<1000\,\mathrm{m}$) or biomass–burning smoke in the free atmosphere (FT, $>1000\,\mathrm{m}$). Other aerosol particles can be neglected. Values used for the particle separation discussed in Sect. 6.2 are given in Table 3.1. Since AERONET shows similar particle size distributions for mineral dust and marine particles, the conversion factor marine particles is assumed to be the same as for mineral dust particles.

Table 3.1: Overview of parameters used for the POLIPHON method for dust (index d), smoke (index FT), and marine (index MBL) particles in terms of the particle depolarization ratio δ, the particle density ρ, the conversion factor ν/τ, and the lidar ratio S.

Parameter	Value	Reference
δ_{d}	0.31	*Freudenthaler et al.* [2009]
δ_{nd}	0.05	*Müller et al.* [2007a]
ρ_{d}	$2.60\,\mathrm{g\,cm^{-3}}$	*Ansmann et al.* [2012]
$\rho_{\mathrm{nd,FT}}$	$1.55\,\mathrm{g\,cm^{-3}}$	*Ansmann et al.* [2012]
$\rho_{\mathrm{nd,MBL}}$	$1.20\,\mathrm{g\,cm^{-3}}$	*Ansmann et al.* [2012]
$\nu_{\mathrm{d}}/\tau_{\mathrm{d}}$	$0.75\times10^{-6}\,\mathrm{m}$	*Ansmann et al.* [2012]
$\nu_{\mathrm{nd}}/\tau_{\mathrm{nd,FT}}$	$0.18\times10^{-6}\,\mathrm{m}$	*Ansmann et al.* [2012]
$\nu_{\mathrm{nd}}/\tau_{\mathrm{nd,MBL}}$	$0.75\times10^{-6}\,\mathrm{m}$	*Albert Ansmann, personal communication,* (April, 2015)
S_{d}	$50\,\mathrm{sr}$	*Tesche et al.* [2009a]
$S_{\mathrm{nd,FT}}$	$80\,\mathrm{sr}$	*Tesche et al.* [2009a]
$S_{\mathrm{nd,MBL}}$	$20\,\mathrm{sr}$	*Groß et al.* [2011]

Chapter 4

Measurement instruments

4.1 Equipment aboard RV Meteor

For routine ship-based cruises (regularly with the ice breaker RV Polarstern), the Leibniz In-
stitute for Tropospheric Research Leipzig (TROPOS) developed the OCEANET measurement
container. This mobile platform has been equipped with several measurement instruments
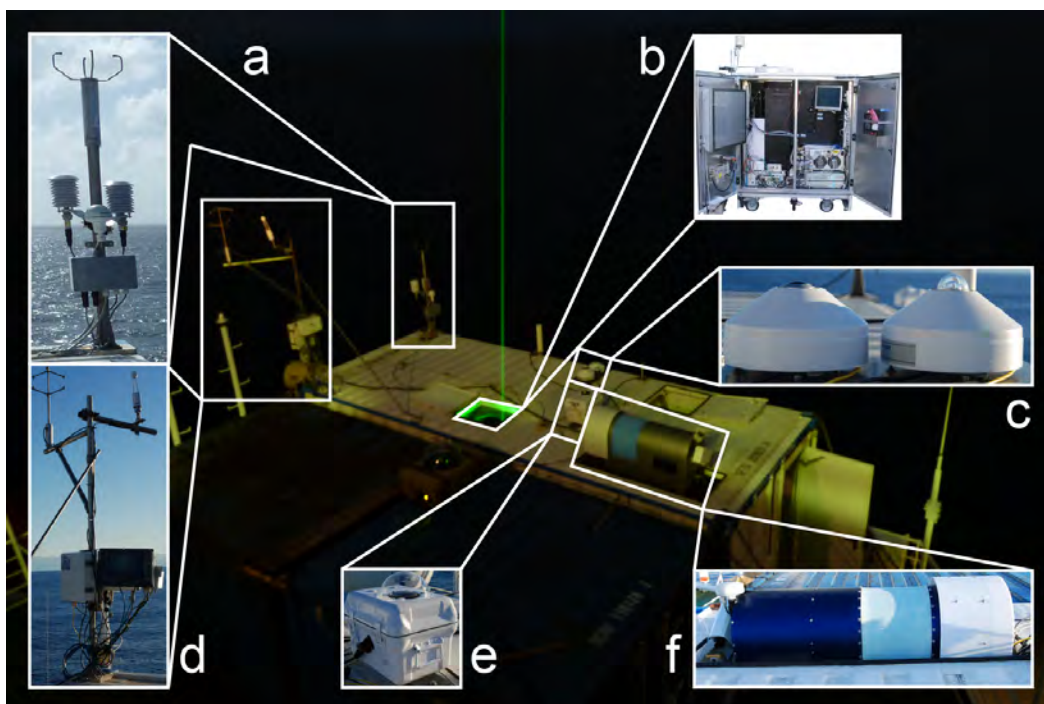as shown in Fig. (4.1) below.

Figure 4.1: Measurement instruments aboard the research vessel Meteor (image created by
Thomas Kanitz). The OCEANET-Atmosphere platform includes instruments for measuring stan-
dard meteorological parameters (**a**), Polly^{XT} lidar (**b**), pyranometer and pyrgeometer (**c**), sonic
anemometer and LICOR gas analyzer (**d**), skyimager (**e**) and a microwave radiometer (**f**).

Box a in Fig. 4.1 shows instruments for the retrieval of the standard meteorological para-
meters temperature, relative humidity, and wind, wherefore it became an official part of the
DWD network. Inside the container (box b) the multiwavelength Raman and polarization
lidar Polly^{XT} has been installed for vertical profiling of optical aerosol properties and wa-
ter vapor mixing ratio. Setup and capabilities of this Polly^{XT} will be explained explicitly
in the following section. For detecting incoming solar and thermal radiation a pyranometer
and pyrgeometer, respectively, are placed on top of the container as it can be seen in box
c. Sensible and latent heat fluxes can be derived from the instrumentation for turbulence
and CO_2–flux measurements (Sonic-Anemometer and LICOR gas analyzer, respectively),
shown in box d. Box e shows a fully automated sky imager which takes regularly pic-
tures of the hemisphere above the platform to enable the estimation of cloud coverage and
cloud type. Finally, in box f a passive microwave radiometer (Humidity And Temperature
Profiler, HATPRO) is displayed. Its data of temperature and humidity profiles enable the
calculation of the liquid-water path (LWP) of the air column above the platform for further
investigations. Not included in Fig. 4.1 is the microtops II sun–photometer (see *Nisantzi
et al.* [2015]), which is operated by the Maritime Aerosol Network (MAN, *Smirnov et al.*
[2009]) component of AERONET. It provides aerosol optical properties at 440, 500, 675,
870, and 936 nm. In this work, we will use the microtops II 440-870 nm Ångström expo-
nent and 500 nm aerosol optical depth (also aerosol optical thickness, AOT) measurements,
which provides information about the aerosol content of the same atmospheric column (see
http://aeronet.gsfc.nasa.gov/new_ web/maritime_ aerosol_ network.html). In addition to the
shipborne observations radiosondes have been launched regularly.

4.2   Polly^{XT} lidar

The multiwavelength Raman and polarization lidar Polly^{XT} (Portable Lidar System Ex-
tended) is the second generation of the portable aerosol Raman lidar system (Polly). This
version includes an extra near-range receiver to enable measurements close to the lidar down
to 120 m above ground, i.e. in our case of the shallow marine boundary layer below 500–700 m
height. It emits light at three wavelengths and has eight detection channels plus two chan-
nels for the near-range signal. Hence, this Polly^{XT} is called a 3+2+2+1+2 system for the
backscatter coefficient can be determined at three wavelength, the extinction coefficient and
the depolarization ratio at two wavelengths, the water vapor content at one wavelength, and
both backscatter and extinction coefficient at one wavelength with the near-range channel.
Figure 4.2 shows the optical setup consisting of emitter (notation 'E') and receiver (notation
'R') component parts. Despite some upgrades, including the near-range receiver, this system
resembles the one described in *Althausen et al.* [2009] and *Engelmann et al.* [2015]. The
following information about technical details are extracted from these publications without
further quoting.
Light pulses at 1064 nm are generated by the Nd:YAG laser (E1 in Fig. 4.2) with a repetition
rate of 20 Hz and an energy of 450 mJ per pulse. The emitted laser beam has a divergence of

less than 1.5 mrad. By the use of mirrors the light is directed to the second and third harmonic crystals (E2) where it is transformed into pulses at wavelength 1064 nm, 532 nm and 355 nm of 180 mJ, 110 mJ, and 60 mJ, respectively. The UV component is measured by an external power meter (E2a) for later quality control. The generated pulses at all wavelengths are linearly polarized by the use of a waveplate and a Brewster–cut Glan–Laser polarizer (E3). Again, by the use of mirrors the beam is turned into the upward direction. An additional shutter (E4) is implemented to stop the laser light emission during airplane overflights. Before the emission, the beam is enlarged in diameter from about 6 to about 45 mm by an achromatic beam expander (E5). With a beam divergence of less than 0.2 mrad the beam is transferred into the atmosphere.
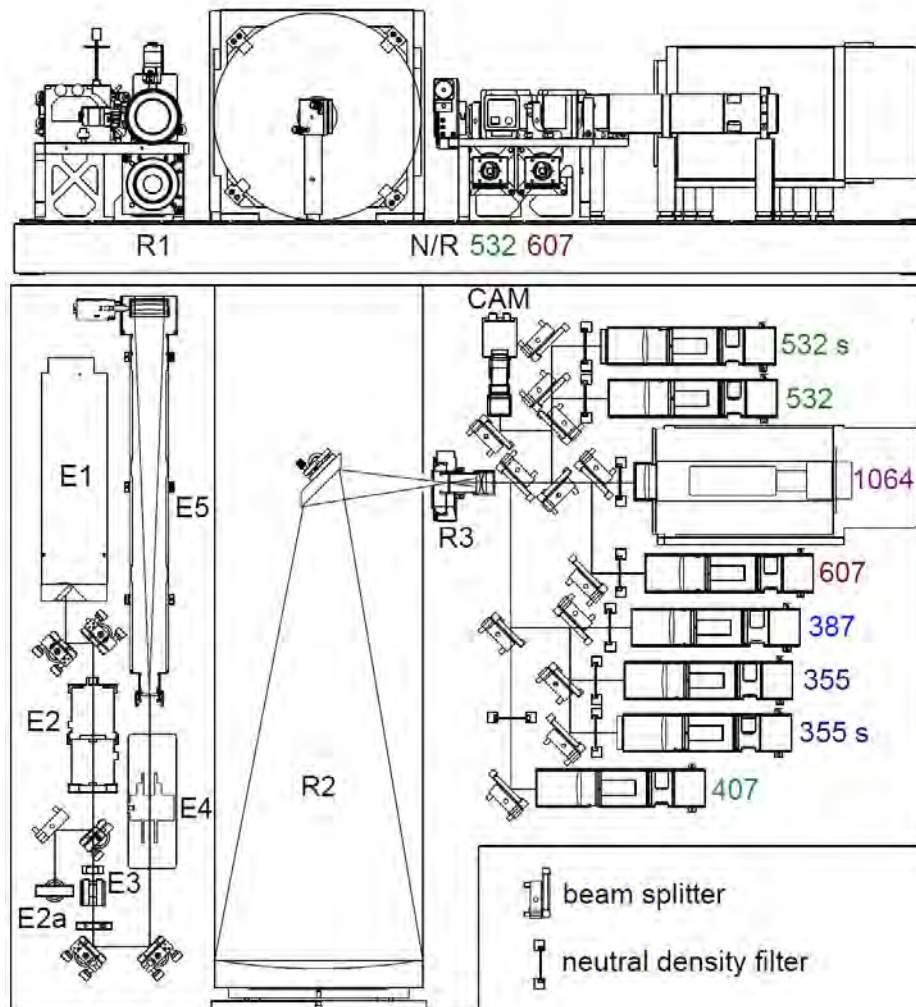
Figure 4.2: Optical setup of the Polly^{XT} lidar. The upper part displays the top view and the lower part the front view. Notations 'E' and 'R' indicate the emitter and receiver unit, respectively. N/R denotes the near-range receiver unit. E1: Nd:YAG laser, E2: second and third harmonic crystal, E3: polarizer, E4: shutter, E5: beam expander, R1 and R2: primary and secondary mirror, R3: pinhole, CAM: camera.

Backscattered light is collected by the receiver units. As mentioned above the Polly^{XT} system developed for the mobile sea facility OCEANET–Atmosphere [*Kanitz et al.*, 2013] includes a far–range and an additional near–range receiver. The far–range receiver unit includes a Newtonian telescope with a primary mirror (R2) of 300 mm in diameter. The pinhole (R3) defines the receiver field of view (RFOV) of 1 mrad. Behind the pinhole an achromatic lens collimates and transmits the light to the seven detection channels and a camera (CAM). Dichroitic beamsplitters separate the light according to its wavelengths. Polarizers are placed in front of the 355 nm and 532 nm-channel, respectively, to ensure detection of cross-polarized light at channels 355s and 532s only. After passing a neutral-density filter, an interference filter, and a focusing lens, the photons in each channel are detected by photomultiplier tubes (PMT) working in photon-counting mode. The signals of the photon-counting PMTs are adapted to the data acquisition (DAQ) cards by preamplifiers. Thus, the signal can be electronically recorded.

The separate near-range receiver operates likewise with a refracting telescope diameter of 50 mm. It is mounted at a close distance of 120 mm from the laser beam axis. The RFOV of the near–range receiver is 2.2 mrad. Simulations show a complete overlap can be calculated approximately 120 m above the lidar. Table 4.1 gives an overview of the detected Polly^{XT} signals. With this Raman lidar the inelastic backscatter signal caused by vibrational-rotational Raman scattering from nitrogen (387 nm and 607 nm for a stimulation wavelength of 355 nm and 532 nm, respectively) and water-vapor (407 nm for a stimulation wavelength of 355 nm) is measured in addition to the elastic backscatter signal. Using the total P and cross–polarized $P^{\perp}$ signals of the 355 and 532, and 355s and 532s channels, respectively, the corresponding parallel–polarized components $P^{\parallel}$ can be calculated (see e.g. *Freudenthaler et al.* [2009]). These Polly^{XT} outputs allow the determination of the particle backscatter and extinction coefficients at 355, 532, and 1064 nm, and 355 and 532 nm, respectively, the lidar ratio at 355 and 532 nm, the backscatter-related Ångström exponent at 355/532 nm and 532/1064 nm,

Table 4.1: Listing of Polly^{XT} detected signals indicating type of scattering and state of polarization.

Channel notation	Detected backscatter signal
355	elastic
355s	cross-polarized elastic
387	N_2 Raman
407	H_2O Raman
532	elastic
532s	cross-polarized elastic
607	N_2 Raman
1064	elastic
N/R 532	elastic
N/R 607	N_2 Raman

the extinction-related Ångström exponent at 355/532 nm, the particle linear depolarization ratio at 355, and 532 nm, as well as the water-vapor mixing ratio by means of the Raman channels (407 and 387 nm).

The lidar component devices are installed on an optical board which is tilted by 5° to avoid depolarization measurement disturbances caused by horizontally aligned ice crystals [*Seifert et al.*, 2010]. The system is powered by an uninterruptible power supply which guarantees a steady power supply for the computer and the laser. In case of rain events, a signal is sent to the computer which stops the laser, and thus pauses the measurement. The automated, continuous measurements can be controlled remotely via internet. According to the measuring schedule, the DAQ software starts the laser, monitors the system status, starts data acquisition, and records the data.

Chapter 5

Dust modeling

Simulations of the spatiotemporal mineral dust distribution by regional transport models can be used to examine the dust transport with sources and sinks. The complex aerosol dynamics and physical, as well as chemical interactions, can be analyzed by means of meso-scale models. Measurement data such as the ship–based lidar measurements, presented in chapter 6, help to evaluate those simulations and to improve dust mobilization parametrization. Also they enable the validation of transport models in terms of the dust emission, transport, and deposition.

The following sections will introduce the models NMMB/BSC–Dust, SKIRON, and MACC. Information about the models are extracted from the websites quoted in each section if not otherwise cited in the text.

5.1 SKIRON

There are more regional dust prediction systems for the Saharan region. Some of them are based on a modified version of the Eta model [*Mesinger*, 1997], a dust module which was created by *Nickovic and Dobricic* [1996]. To these belong the dust model SKIRON developed at the University of Athens [*Rodriguez et al.*, 2001; *Kallos et al.*, 2006], and the regional dust model DREAM ('Dust Regional Atmospheric Model') [*Nickovic et al.*, 2001] which is used by the ICoD ('Euro-Mediterranean Center on Insular Cloud Dynamics'). The latest version of these models implement complex parametrizations by *Nickovic et al.* [2001] and provide size resolved dust distributions of 4 (SKIRON) [*Kallos et al.*, 2006] and 8 (DREAM) [*Pérez et al.*, 2006] size channels, respectively.

SKIRON (*http://pandora.meng.auth.gr/mds/showlong.php?id=175*) is a non hydrostatic 3D model based on the Eta/NCEP (National Centers for Environmental Prediction) atmosphere model [*Kallos et al.*, 1997]. The system consists of two major parts: the modified Eta/NCEP and the dust modules. Detailed descriptions of dynamics and physical components of the Eta model can be found in the studies of *Mesinger et al.* [1988] and *Janjic* [1994]. The models temporal resolution is 1 hour. Predictions can be made for intervals up to 5 days. The horizontal spatial resolution yields 0.24 x 0.24 degrees at a vertical separation in 38 height levels from

the earth surface up to 22 km height. Horizontal advection and convection are represented by a Eta/NCEP model scheme for the advection of passive substances [*Janjic*, 1997]. Vertically considered both processes follow a scheme by *van Leer* [1977]. A second-order diffusion scheme is used to depict horizontal diffusion by adjusting the Smagorinsky coefficient by the use of the model term for turbulent kinetic energy [*Janjic*, 1990]. Deposition is also modeled in SKIRON. Dry deposition of particles by diffusion, impaction, or gravitation follows approaches by *Slinn and Slinn* [1980]. Wet deposition above and underneath clouds is described by *Seinfeld and Pandis* [1998]. Chemical processes are not implemented in SKIRON. Output variable are: dust concentration, dust load, dust deposition (wet and dry), aerosol optical depth, air pressure asl, wind field, temperature and geopotential height at 500hPa, 700hPa, 850hPa. Those quantities can be derived for the regions of the Mediterranean Region-Europe and the North Atlantic.

5.2 NMMB/BSC–Dust

The dust cycle model BSC (Barcelona Supercomputing Center)–Dust is embedded online within the National Centers for Environmental Prediction (NCEP) non–hydrostatic Multiscale Model (NMMB) which has been extended to global scale (*http://www.bsc.es/earth-sciences/mineral-dust/nmmbbsc-dust-forecast* and *http://dust.aemet.es/methods/the-nmmb-bsc-dust-model*). It has been developed at the Earth Sciences Dpt. of the Barcelona Supercomputing Center-Centro Nacional de Supercomputación (BSC-CNS) in collaboration with NOAA/NCEP, NASA Goddard Institute for Space Studies and the International Research Institute for Climate and Society (IRI). Model descriptions are taken from *Pérez et al.* [2011] if not otherwise quoted.

NMMB/BSC-Dust provide short to medium-range dust forecasts for both regional and global domains, and represents a first step towards the development of a unified chemical-weather model. BSC-Dust solves the mass balance equation for dust taking into account: (1) dust generation and uplift by surface wind and turbulence, (2) horizontal and vertical advection, (3) horizontal diffusion and vertical transport by turbulence and convection (4) dry deposition and gravitational settling and (5) wet removal which includes in-cloud and below-cloud scavenging from convective and stratiform clouds. Transport of dust by advection and turbulent diffusion is analogous to those of moisture transport in the NMMB.

The dust emission scheme is physically-based and takes saltation and sandblasting processes into account [*White*, 1979; *Marticorena and Bergametti*, 1995; *Marticorena et al.*, 1997] using a source function after *Ginoux et al.* [2001]. To specify the soil size distribution the soil textures of the hybrid STATSGO-FAO soil map are used. Dust particle size distributions are according to the criteria used in *Tegen et al.* [2002]. Soil wetness effects on dust production are given by *Fécan et al.* [1999]. Horizontal diffusion and vertical transport by turbulence and convection, as well as horizontal and vertical advection follow *Janjic et al.* [2009]. *Zhang et al.* [2001] provides approaches for dry deposition and gravitational settling while wet removal is designed on the basis of *Betts* [1986]; *Betts and Miller* [1986]; *Janjic* [1994]; *Ferrier*

et al. [2002]. To estimate the radiative interactions of aerosols and mineral dust, the rapid
radiative transfer model (RRTM) [*Mlawer et al.*, 1997] is implemented in the model.

5.3   MACC

MACC ('Monitoring Atmospheric Composition & Climate') is an EU project
(*http://www.gmes-atmosphere.eu/about/project/*) directed by the 'European Centre for
Medium-range Weather Forecasts' (ECMWF) in Reading, United Kingdom. It started in
2009 as a preceding service within the Copernicus initiative continuing and refining the pro-
ducts developed in the projects GEMS ('Global and regional Earth-system Monitoring using
Satellite and in-situ data') and PROMOTE. Its services cover air quality, climate forcing,
stratospheric ozone, UV radiation and solar-energy resources. The third phase of funding
MACC-III will end in 2015.
The functionality and an overview of the major data input and general products are shown
in the diagram below.
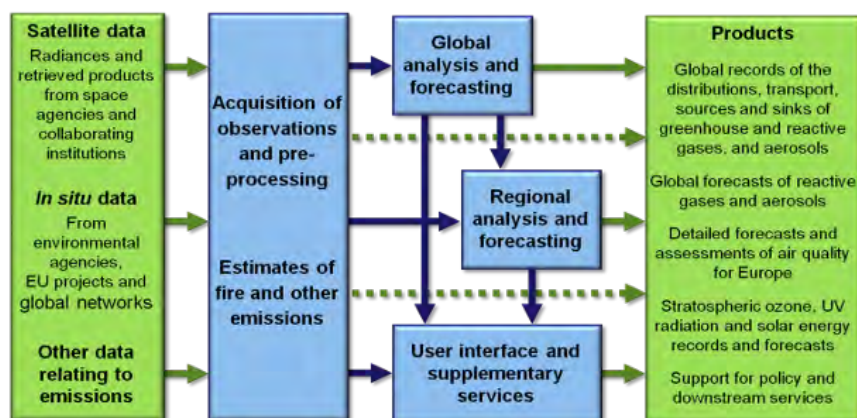
Figure 5.1: Diagram of the MACC project showing input data, structure, data processing and
output components (*https://www.gmes-atmosphere.eu/about/project_ diagram.png*).   Data and
product flows are pointed out by the arrows.

MACC gets input data from satellites, in-situ measurements and information about aerosol
emissions and fires. It derives observational and emission products based on the satellite
data retrievals. For the data processing on a global and regional level, respectively, it also
generates estimates of fire and other emissions as input data.
The main global products in MACC are analyses of greenhouse gases, reactive gases and
aerosols, produced in near-real-time and retrospective modes. It also estimates climate forc-
ing and emissions and sinks and forecasts reactive gases and aerosols. At the regional level
which is focused on Europe MACC provides multi-model forecasts and assessments of air
quality using regional systems and services for stratospheric ozone, UV radiation and so-
lar energy. Those products are freely available at the project homepage *http://www.gmes-
atmosphere.eu/*.

Chapter 6

Experiment, results, and discussion

6.1 Measurement overview

The transatlantic cruise M96 of the German RV Meteor took place from 29 April to 23 May 2013 starting at Guadeloupe (16° N, 61° W) and ending at Cape Verde (17° N, 25° W) covering a distance of approximately 4000 km. The cruise track can be seen in Fig. 6.1. The OCEANET container was aboard including a new Polly^{XT}. The lidar performed continuous observations, and thus enabled the determination the optical properties of the lofted aerosol layers during the cruise.
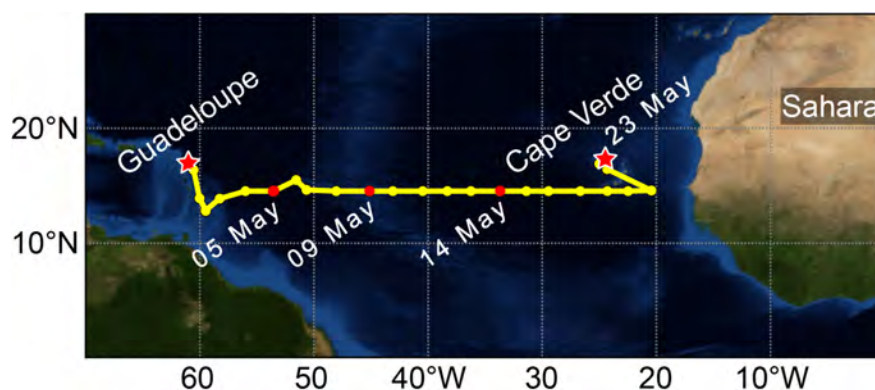
Figure 6.1: Map showing the North Atlantic Ocean. The cruise track of the RV Meteor from Guadeloupe (29 April 2013) to Cape Verde (23 May 2013) is plotted as a yellow line [*Kanitz et al.*, 2014]. Dates of case studies are marked by red and the right red star.

Kanitz et al. [2014] provided an overview and first results of the lidar measurements. Two case studies were discussed in detail. Figure 6.2 from that work shows the 1064 nm range corrected backscatter signal (a), and the 532 nm volume depolarization ratio (b) for all measurements of the cruise between 2 May and 23 May 2013. The high backscatter signal (red and orange color in Fig. 6.2a) in the near range of the lidar indicates the marine boundary layer (MBL). The MBL top height varied between 300 and 1700 m height. Green and yellow

colors indicate lofted dust up to 5 km height in the period from 9–23 May 2013, and also an aged dust plume up to 2.5 km height from 4–6 May 2013. This is corroborated by the increased volume depolarization ratio in these layers (Fig. 6.2b, yellow to red colors) which indicates the presence of non–spherical scatterers such as mineral dust particles. This is consistent with lidar observations during the summer campaign of SAMUM–2 at Cape Verde from 24 May to 17 June 2008 where dust depolarization ratios at 532 nm of 0.31±0.10 [*Tesche et al.*, 2011] were observed up to 5 km height above the MBL. In contrast to this, the MBL is characterized by low depolarization ratios <0.5 [*Tesche et al.*, 2011; *Groß et al.*, 2011].
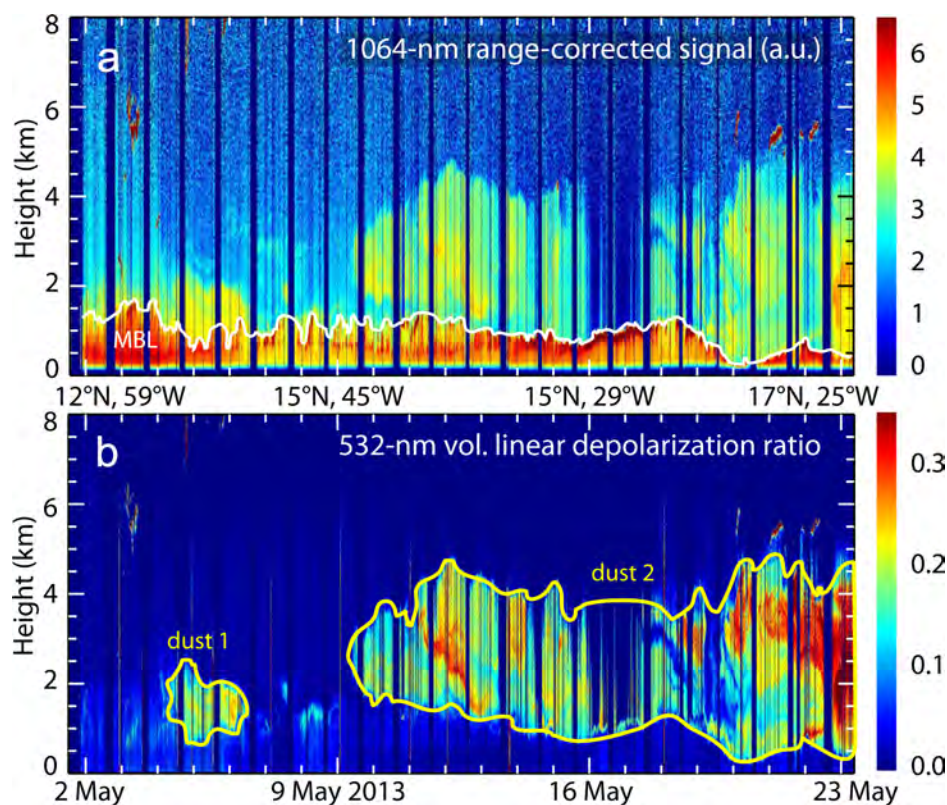
Figure 6.2: Composite of lidar measurement height versus time displays during the RV Meteor cruise of (**a**) range–corrected backscatter signal at 1064 nm, and (**b**) the volume depolarization ratio at 532 nm. Measurement breaks around 1200 LT (blue vertical lines) are due to high sun elevation. The marine boundary layer (MBL) top is indicated by a white line in **a** and layers containing non–spherical dust particles are highlighted by yellow lines in **b** (*adopted from Kanitz et al.* [2014]).

In addition to that, the aerosol optical thickness (AOT) has been measured by the hand-held AERONET–MAN microtops sun–photometer. The daily mean AOT at 500 nm and the Ångström exponent calculated from sun photometer measurements at 440 and 870 nm (eq. 3.13) are shown in Fig. 6.3 (orange and blue dots, respectively). Those mean AOT values varied between 0.08 (typical remote Atlantic AOT, see *Smirnov et al.* [2009]) and 0.7 on 7 and 23 May 2013, respectively. The Ångström exponent assumed values of about 0.7 when the AOT was lowest, confirming the dominance of sea salt particles, and close to zero when the

AOT was highest and large dust particles are expected (reconsidered in Sect. 6.4). During the presence of dust plumes the mean AOT was 0.2–0.3 representing large sea salt particles and mineral dust [*Tesche et al.*, 2011]. However, the mean Ångström exponent varied significantly between those two dust periods from 0.28 in the short-term transported dust layer to 0.5 in the aged dust plume (shaded gray in Fig. 6.3). This shows that less or smaller dust particles seem to be present and fine mode particles dominate the aerosol mixture in the processed aerosol layer. The corresponding mean AOT were 0.3 and 0.2, respectively.
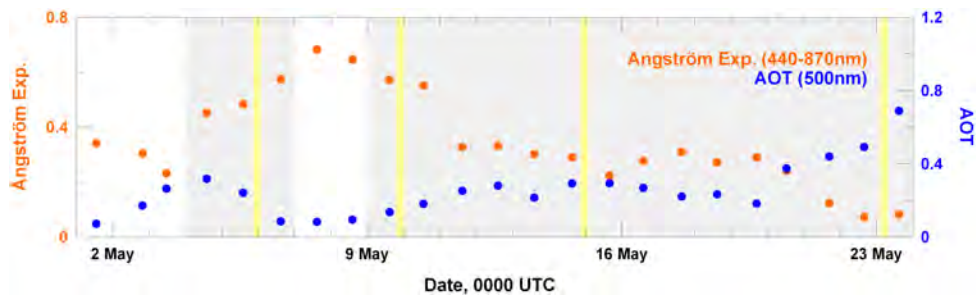
Figure 6.3: Time series of daily averaged sun–photometer observations aboard RV Meteor of aerosol optical thickness (AOT) at 500 nm (blue dots) and Ångström exponent derived from 440–870 nm wavelength (orange dots) for the 29 April–24 May 2013 period (see *http://aeronet.gsfc.nasa.gov/new_web/cruises_new/Meteor_13_1.html*, Level 2.0 AOD). Gray shades indicate dust episodes and yellow lines show dates of case studies discussed in the next section.

6.2   Case studies

The late evening measurements of 5 May (2340–0035 UTC), 9 May (2315–2400 UTC), 14 May (2345–0020 UTC) and early morning measurements of 23 May 2013 (0345–0500 UTC) have been used as the data base for a detailed discussion of the optical properties of the aerosol in the MBL and the lofted dust plumes. The observation on 5 May shows an aged dust layer (almost 10 days of travel over the ocean, dust 1 in Fig. 6.2), whereas observations on 9 May (4.5 days over the ocean), 14 May (2.5 days over the ocean), and 23 May (1.5 days over water) characterize a less aged dust layer (dust 2 in Fig. 6.2). The profiles of the optical properties derived from the lidar measurements in terms of the backscatter and extinction coefficient, lidar ratio, Ångström exponent, and particle linear depolarization ratio are shown in Fig. 6.4 for all cases. Backward trajectories (Fig. 6.5) are taken into account in the discussion of the case studies. The trajectories are calculated with the Hybrid Single–Particle Lagrangian Integrated Trajectory (HYSPLIT) model (for further information see *http://www.arl.noaa.gov/HYSPLIT_info.php*) and are used to estimate travel time and identify aerosol sources which contributed to the observed aerosol plumes.
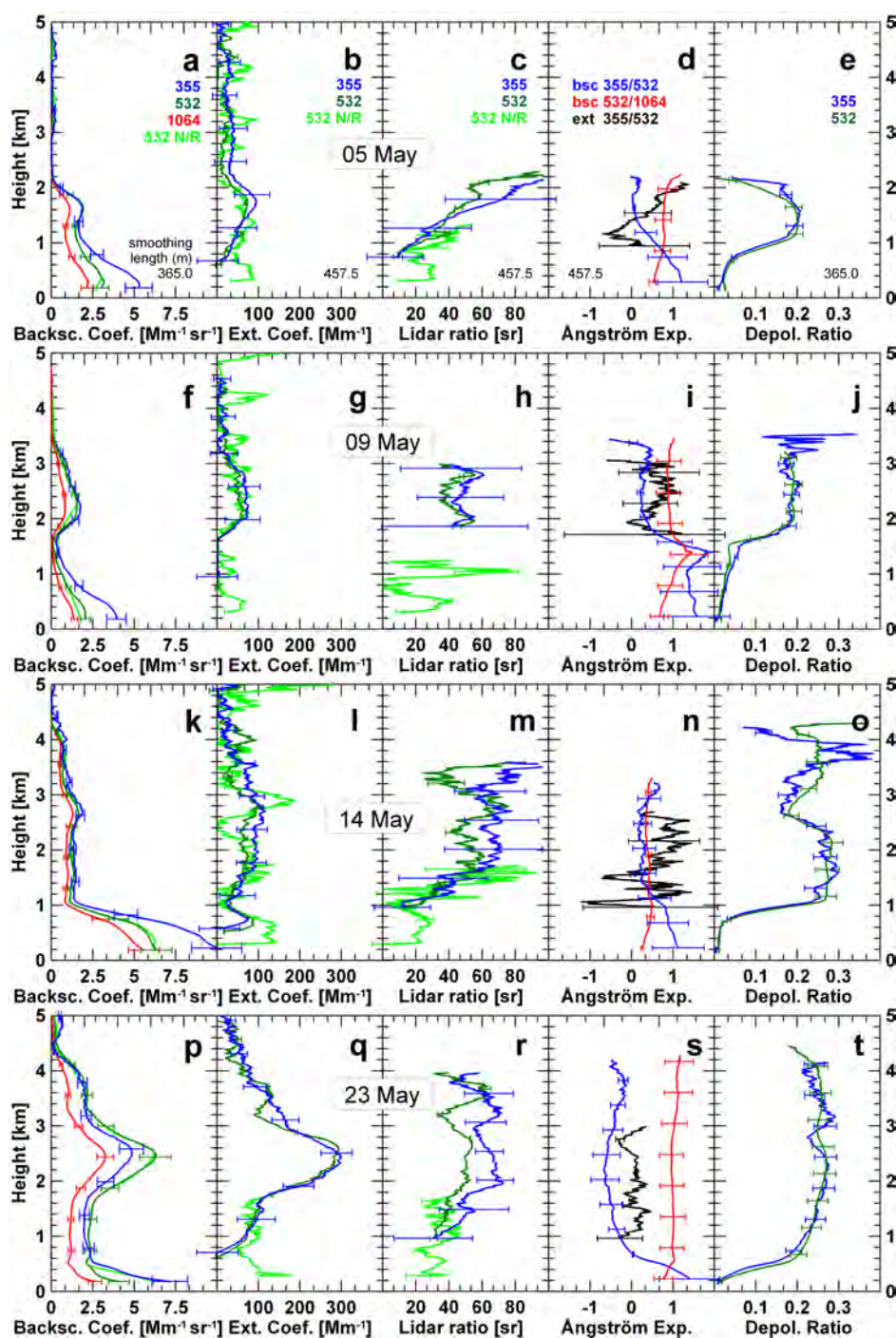
Figure 6.4: Averaged profiles of backscatter (**a**) and extinction (**b**) coefficient, lidar ratio (**c**), Ångström exponent (**d**), and particle linear depolarization ratio (**e**) as determined on 05 May 2013, 2340–0035 UTC. The same in **f**–**j** for 09 May 2013, 2315–2400 UTC, **k**–**o** for 14 May 2013, 2345–0020 UTC, and **p**–**t** for 23 May 2013, 0345–0500 UTC. The label N/R denotes the near-range receiver channel. The signal smoothing length for the profiles of backscatter coefficient and particle linear depolarization ratio is 365.0 m. Lidar signals are vertically smoothed with 457.5 m before the computation of extinction coefficients, lidar ratios, and Ångström exponents.
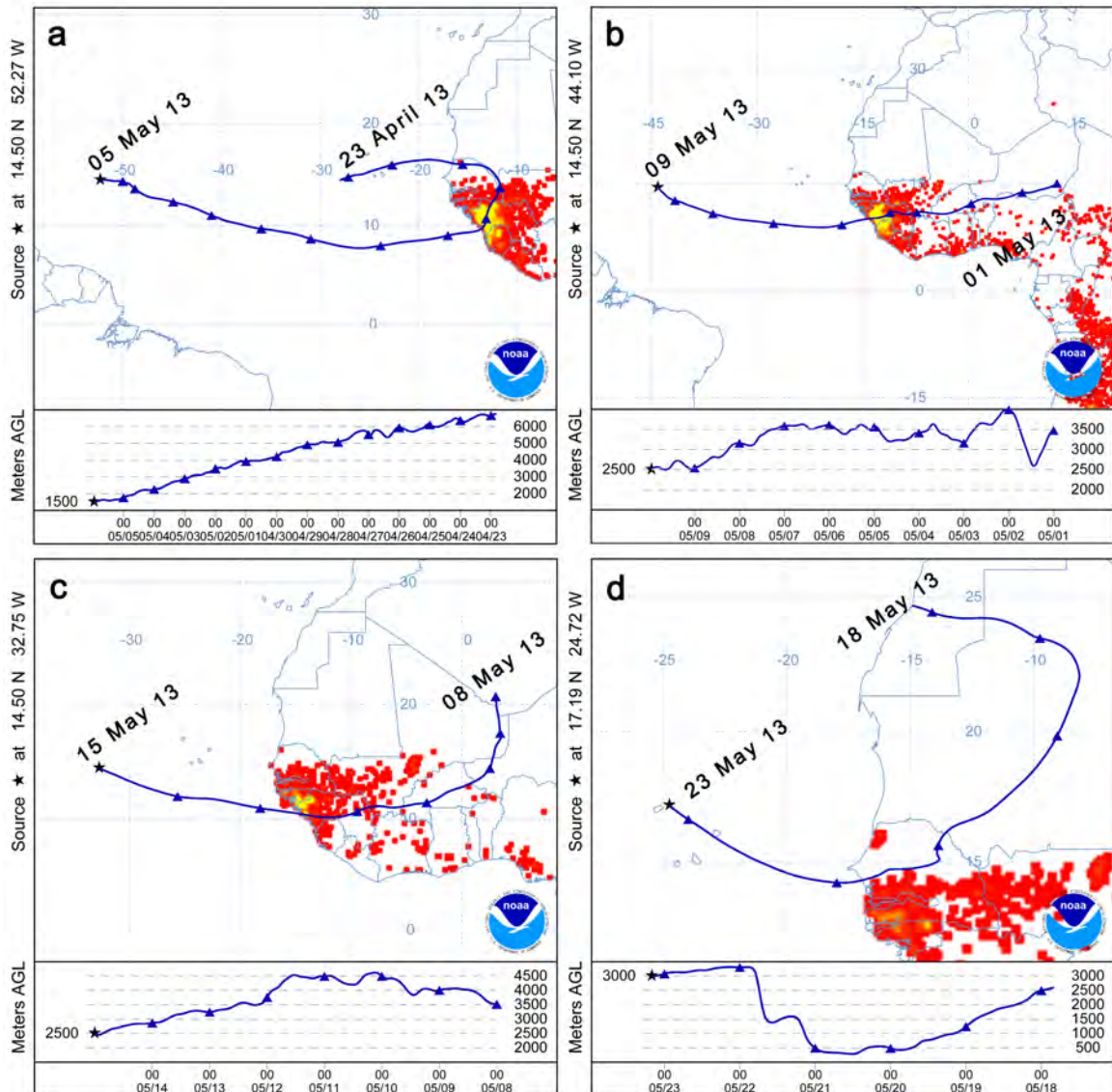
Figure 6.5: Backward trajectories for one height level (center of the lofted dust layer) ending at 05 May 2013, 2300 UTC (**a**), 09 May 2013, 2300 UTC (**b**), 14 May 2013, 2400 UTC (**c**), and 23 May 2013, 0400 UTC (**d**), respectively. Symbols at the trajectories indicate the residence time in days. Calculations are performed with the NOAA HYSPLIT model using GDAS meteorological data (http://ready.arl.noaa.gov/HYSPLIT_traj.php). In addition fires detected by MODIS on board the Terra and Aqua satellites are shown accumulated over a 10-day period (1–10 May 2013 for **a** and **b**, 21–30 May 2013 for **c** and **d**) (http://rapidfire.sci.gsfc.nasa.gov/firemaps). Color ranges from red (low number of fires) to yellow (high number of fires).

05 May 2013

The lidar observations during the night of 5–6 May 2013 are shown in Fig. 6.6. It documents a marine boundary layer top height of 500–1000 m characterized by low depolarization ratio (Fig. 6.6b). Low–level clouds are present in the MBL around the 2340–0035 UTC time period, which was selected for the case study. Above, an aerosol layer stretches up to 2 km height. HYSPLIT-backward trajectories for this observed layer indicate a transport time of 10–11 days (see Fig. 6.5a, top). According to calculated heights at which the aerosol was transported before the observation, the air masses may have never been close to the ground (Fig. 6.5a, bottom) and also did not pass the Saharan desert region, but areas of considerable amount of active fires (red to yellow colors in Fig. 6.5a, top) at great heights of 5–6 km above ground. Thus, only a little amount of Saharan dessert dust may be expected in these layers. Day sun–photometer AOT measurements of 0.25 (Fig. 6.3) are in in good agreement with optical depth from the 532 nm extinction profile of 0.23. The lidar-derived optical depth was obtained
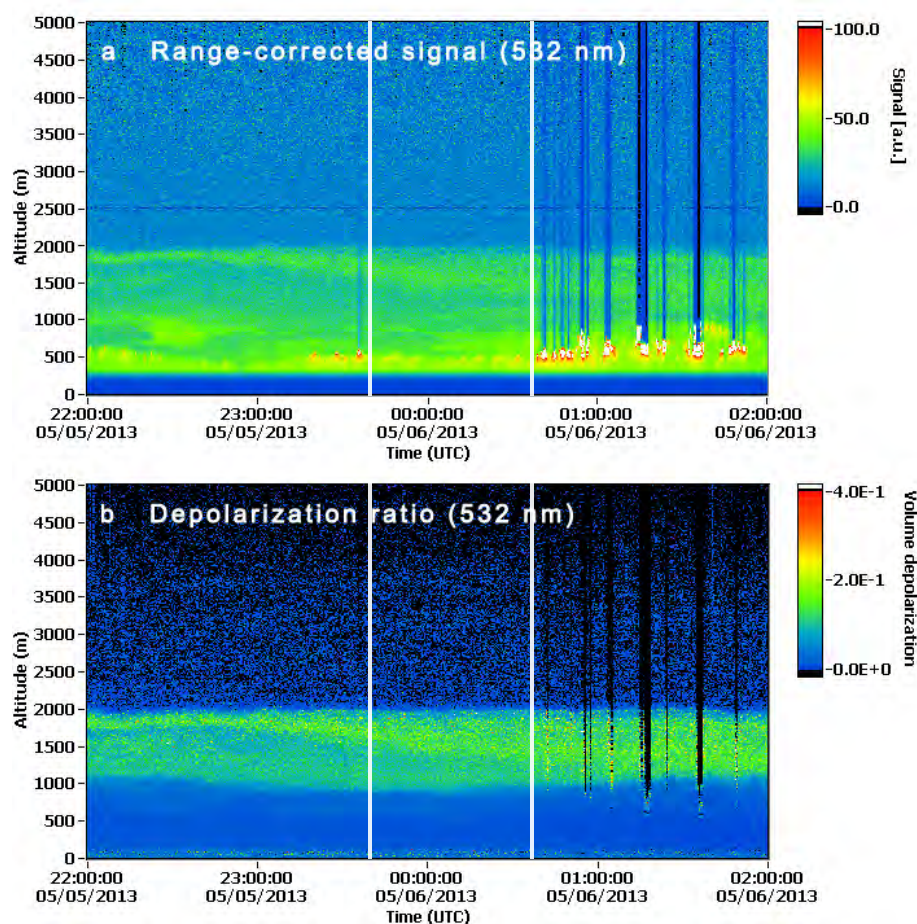
Figure 6.6: Lidar observations on 05–06 May 2013, 2200–0200 UTC. The 532 nm range-corrected signal (**a**) and the 532 nm linear volume depolarization ratio (**b**) are shown. Vertical lines indicate the signal averaging period for which the profiles of optical properties in Fig. 6.4a–e are calculated.

from integration of the 532 nm extinction coefficient in the height range from 1 to 7 km height (see Eq. 3.14). The optical properties derived from the lidar measurements on 05 May 2013, 2340–0035 UTC are shown in Fig. 6.4a–e. Profiles are smoothed with a window length of 457.5 m, except for backscatter and depolarization ratio profiles which are smoothed with 365.0 m window length. The main layer between 1–2 km is characterized by height constant depolarization ratios of about 20 % at both wavelengths which indicates a well-mixed layer of dust and smoke. Wavelength independence of the particle depolarization ratio has also been found during SAMUM–2 (see *Tesche et al.* [2011]). This increased depolarization ratio and almost wavelength–independent extinction coefficients at 74±31 and 66±19 Mm^{-1} at 355 and 532 nm indicate the presence of mineral dust[*Kanitz et al.*, 2013]. All in all, the N/R 532 nm extinction coefficient profile is in good agreement with the profile of the 532 nm extinction coefficient. For heights above 1.5 km, the 355 nm extinction coefficient profile deviates significantly from the 532 nm extinction coefficient. Both extinction coefficients show unusual high values above the detected aerosol layer. These facts might be due to overlap problems and leads to increased lidar ratios and extinction related Ångström exponent (see 6.4c–d) above 1.5 km height. The mean lidar ratio is 43±17 and 40±19 sr at 355 and 532 nm, respectively. These values are lower than typical values for pure Saharan dust (50–60 sr, *Groß et al.* [2011], *Freudenthaler et al.* [2009]). This may result from aged fine–mode smoke or marine particles. Figure 6.4d shows mean extinction and backscatter–related Ångström exponents of 0.3±0.6 and 0.1±0.1 (355/532 nm), respectively, which suggests large particles in this layer. The mean backscatter–related Ångström exponent for 532/1064 nm wavelength is 0.8±0.0 and sun–photometer measurements show an Ångström exponent of 0.5 for the 440–870 nm wavelength range (Fig. 6.3).

09 May 2013

The night measurement of 9 May 2013 2315–2400 UTC is shown in Fig. 6.7. In the display of the volume depolarization ratio an aerosol layer stretches from 1.8 to 3.2 km height. The air mass left the African continent about 5 days before (Fig. 6.5b). Again, the convective MBL below is characterized by a low depolarization ratio. MODIS fire detection shows strong active fires along the HYSPLIT transport route of the lofted layer south of the Saharan desert. Profiles corresponding to the 2315–2400 UTC time period in Fig. 6.4f–j show the main layer extended from 1.8–3.2 km. The height-constant value of the particle depolarization ratio in the 1.8—3.2 km layer indicates that this layer was well mixed (Fig. 6.4j). Like in the first case study the depolarization ratios are 20 % at both 355 and 532 nm wavelength. This value is considerably lower than typical values for pure dust of ∼0.3 (see e.g. *Freudenthaler et al.* [2009], *Groß et al.* [2011], *Tesche et al.* [2011]) and indicates a mixture of dust and smoke or marine particles. Extinction coefficients of 70±10 and 54±11 Mm^{-1} at 355 and 532 nm and mean lidar ratios of 50±10 and 43±12 sr at 355 and 532 nm are also similar to the first case. However, the AOT is lower with values of 0.15 and 0.14 for sun–photometer and lidar measurements, respectively. As can be seen in Fig. 6.4i, the extinction–related Ångström exponent is 0.7±0.5. Backscatter–related Ångström exponents are 0.3±0.1 and
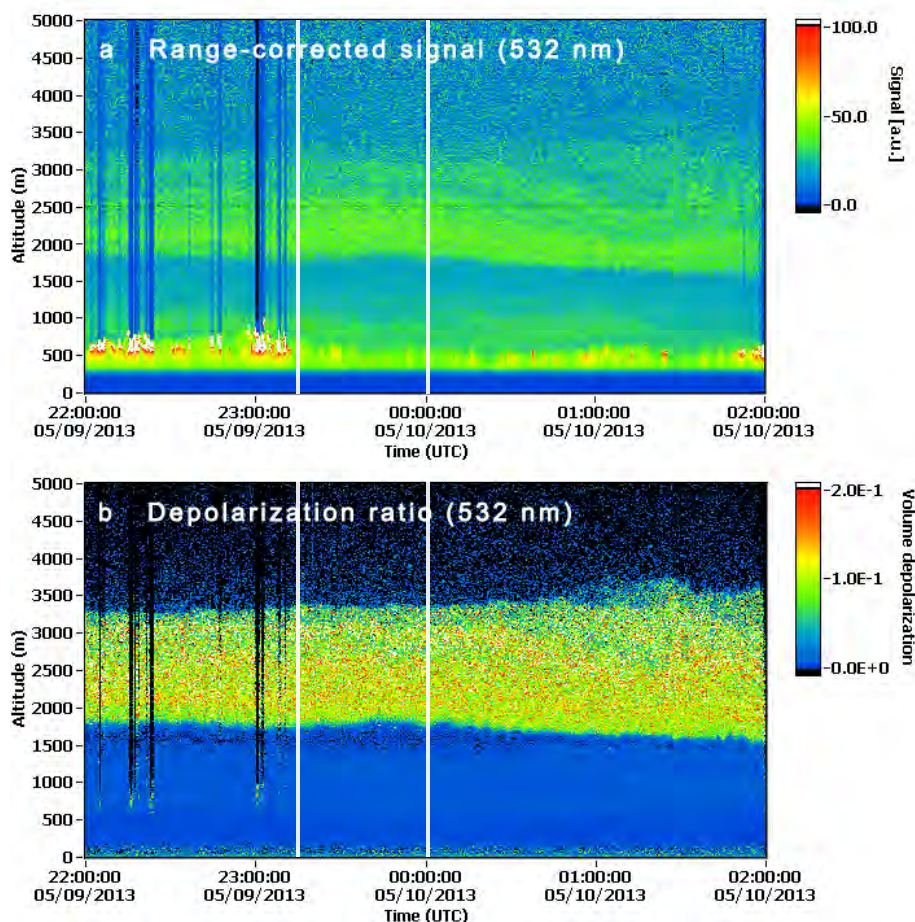
Figure 6.7: Same as Fig. 6.6 but for the night measurement on 09 May 2013, 2315–2400 UTC.

0.9±0.0 at 355/532 nm and 532/1064 nm, respectively. Sun–photometer measurements show an Ångström exponent of 0.55 at 440–870 nm (Fig. 6.3).

14 May 2013

Westward transported mineral dust layers were observed in the height range from 1–4 km in the night of 14–15 May 2013 (see Fig. 6.8b). These layers are best visible in the depolarization ratio panel while the range-corrected signal in these heights shows low values above 1 km. The atmospheric residence time of the lofted aerosol layers over the ocean was about 2.5 days (Fig. 6.5c). The air masses originated from the center of the Saharan desert and passed active fires during transport. Again, the AOT of sun–photometer and lidar measurement are consistent with values about 0.3. Profiles of the optical properties on 14 May 2345–0020 UTC are shown in Fig. 6.4k–o. In this case study the depolarization ratio is not height constant and shows a minimum of about 20% between 2.5 and 3 km height. At this height range lidar ratios of 355 and 532 nm assume almost equal values of about 65 sr and the backscatter coefficients are slightly increased. The depolarization ratios assume values around 27%
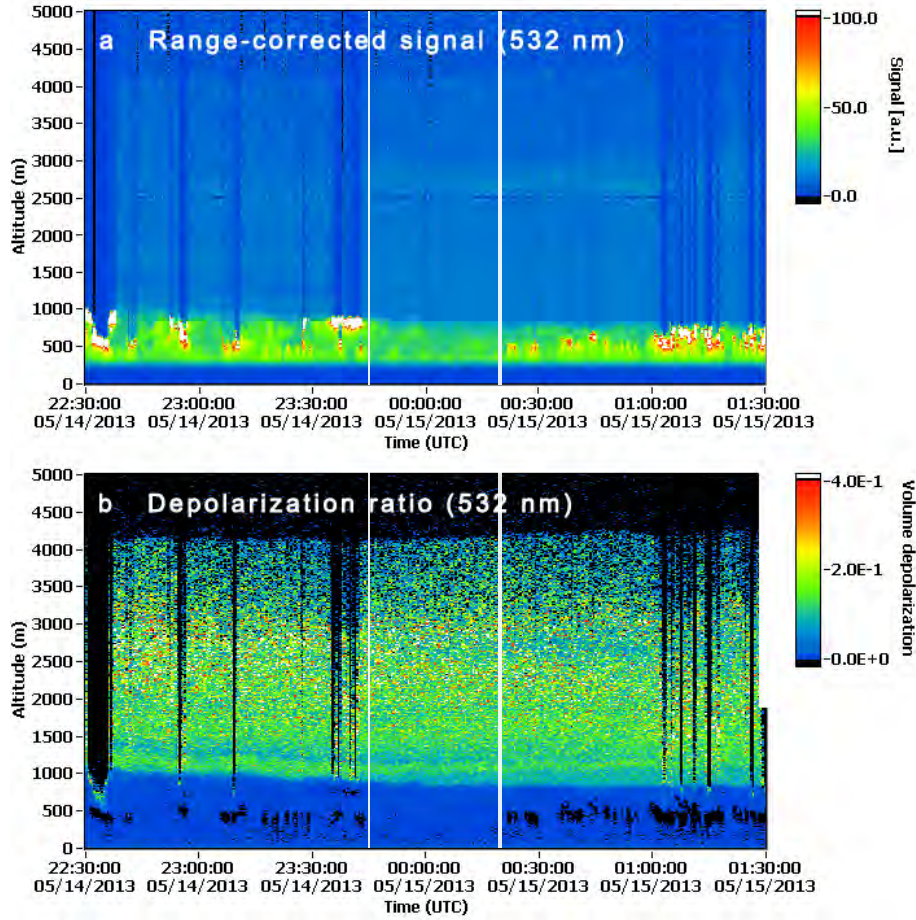
Figure 6.8: Same as Fig. 6.6 but for the night measurement on 14–15 May 2013, 2345–0020 UTC.

throughout the rest of the elevated aerosol layer which indicates almost pure dust conditions. Also the mean lidar ratios of 66±12 and 53±25 sr at 355 and 532 nm are in good agreement with results from the SAMUM campaigns for dust dominated cases [*Tesche et al.*, 2011]. Backscatter coefficients show almost no wavelength dependence. Extinction coefficients are 93±20 and 68±32 Mm^{-1} at 355 and 532 nm, respectively. In the display of the Ångström exponent a good agreement of the backscatter–related 355/532 and 532/1064 nm Ångström exponents is visible with mean values of 0.3±0.2 and 0.4±0.0, respectively. In comparison to the previous case studies the sun–photometer–derived Ångström exponent at 440–870 nm decreased significantly to 0.3 (Fig. 6.3). The extinction Ångström exponent is 0.8±0.7.

23 May 2013

Fig. 6.9 shows the time–height displays of the range–corrected signal and the volume depolarization ratio measured with Polly$^{\text{XT}}$ in the morning of 23 May 2013. The MBL reached heights up to 350–500 m. The strong volume depolarization ratio clearly indicates a dust containing aerosol layer stretching up to 4.2 km height (Fig. 6.9b). The ratio increases with
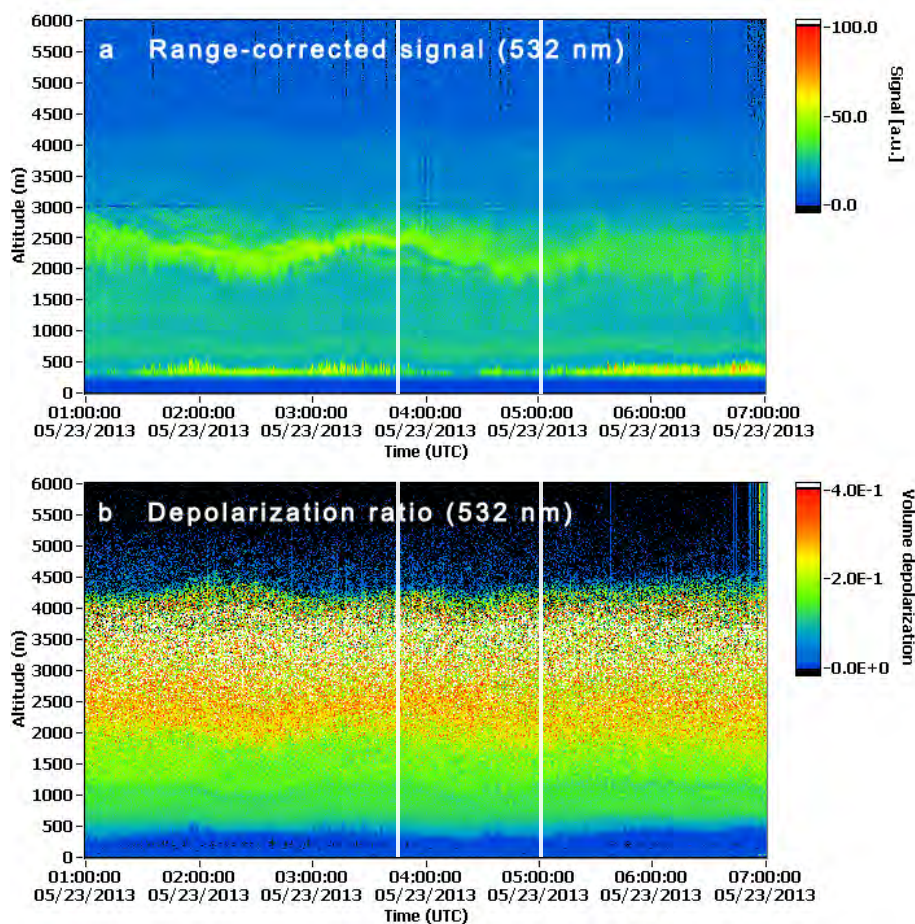
Figure 6.9: Same as Fig. 6.6 but for the morning measurement on 23 May 2013, 0345–0500 UTC.

height and has its maximum around 3.5 km above ground. As can be seen in Fig. 6.5d, dust in the air parcel observed at 3 km height above the measurement instrument was advected from Mauritania. The trajectory in this layer was over desert areas for almost 3 days before reaching ground level at semidesert and steppe regions. The air masses traveled over the Atlantic Ocean for roughly 2 days before the lidar observation. The upper panel in Fig. 6.9a shows a strong signal band around 2.5 km height. This is also visible in the 0345–0500 UTC profiles (Fig. 6.4p–t). Both backscatter and extinction coefficients have their maximum at that height. Again, no wavelength dependence of light extinction is visible with maximum values of $300\,\mathrm{Mm}^{-1}$ and mean values of 178 ± 74 and $169\pm82\,\mathrm{Mm}^{-1}$ at 355 and 532 nm, respectively. The backscatter coefficient at 532 nm was significantly larger than at 355 nm. The corresponding backscatter–related 355/532 nm Ångström exponent was therefore negative (blue line in Fig. 6.4s). Such an unusual backscatter behavior was also observed during a field campaign in Crete in the summer of 2014 [*Holger Baars*, personal communication, April, 2015]. Mean extinction and backscatter–related 532/1064 nm Ångström exponents are 0.1 ± 0.5 and 1.0 ± 0.1, respectively. The sun–photometer–derived Ångström exponent is 0.06

(see Fig. 6.3). An almost height independent particle depolarization ratio with mean values of 26% at both wavelengths (Fig. 6.4t) indicates a well-mixed dust layer. Corresponding mean lidar ratio of 60±9 and 47±11 sr at 355 and 532 nm are in reasonable agreement to the SAMUM–1 and SAMUM–2b observations for pure dust ($S_d \approx$ 53–61 sr, *Tesche et al.* [2011], *Freudenthaler et al.* [2009], *Groß et al.* [2011]). In comparison to the previous case studies, high AOT (see Fig. 6.3) values of 0.65 and 0.56 were measured with the sun–photometer and lidar, respectively.

The polarization lidar photometer networking (POLIPHON) method introduced to separate light–depolarizing dust (index d) particles from weakly depolarizing non–dust (index nd) particles and to retrieve dust and non–dust mass concentrations has been applied to the four cases under study (see Fig. 6.10 and 6.11). The technique was explained in Sect. 3.8. Figure 6.10 shows the distinct separation steps in terms for the 5 May case. The basic lidar parameters are the particle backscatter coefficient (Fig. 6.10a) and the particle depolarization ratio (Fig. 6.10b). With the dust depolarization ratio $\delta_d = 0.31$ [*Freudenthaler et al.*, 2009] and the non–dust depolarization ratio $\delta_{nd} = 0.05$ [*Müller et al.*, 2007a] the POLIPHON method allows the calculation (see Eq. 3.23) of the profile of the dust backscatter coefficient (orange, Fig. 6.10c). The profile of the non–dust backscatter coefficient (black, Fig. 6.10c) is then obtained from the relation $\beta_{nd} = \beta_{aer} - \beta_d$. It is already visible, that the non–dust particles prevail in the lowermost 1 km, whereas a significant amount of dust particles are present between 800–2000 m height asl. By means of the appropriate lidar ratios of dust, smoke (index
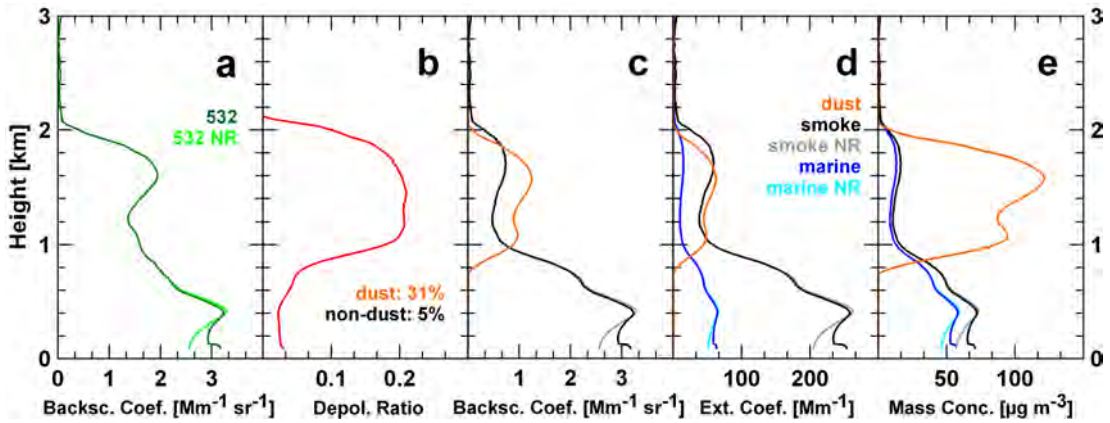

Figure 6.10: (**a**) 532 nm particle backscatter coefficient (green), (**b**) 532 nm particle linear depolarization ratio (red), (**c**) non–dust (black and gray) and dust (orange) particle backscatter coefficients, (**d**) non–dust (black and gray for smoke, blue and cyan for marine particles) and dust (orange) particle extinction coefficients, and (**e**) non–dust (black and gray for smoke, blue and cyan for marine particles) and dust (orange) particle mass concentrations obtained from the POLIPHON method application. The lidar observations were taken on 05 May 2013, 2340 UTC to 0035 UTC.

FT), and marine (index MBL) particles ($S_d = 50\,\text{sr}$, $S_{\text{nd,FT}} = 80\,\text{sr}$, $S_{\text{nd,MBL}} = 20\,\text{sr}$, *Tesche et al.* [2009a], *Groß et al.* [2011]) the profiles of the particle extinction coefficients (Fig. 6.10d) can be estimated. As can be seen in this panel, dust significantly contributes to the total particle extinction coefficient in the free troposphere with values on the order of 50–70 Mm^{-1} (orange line). The same values are obtained for the non–dust component, if we assume that the non–dust aerosol is smoke (black line). Thus, considering the total particle extinction coefficient in Fig. 6.4b which shows values about 70 Mm^{-1}, the dominance of marine particles in the free troposphere is most likely. Finally, the mass concentration profiles are obtained from Eq. 3.24a and 3.24b with characteristic densities and conversion factors for the different aerosol types (shown in Table 3.1).

Same steps have been performed for the remaining case studies (Fig. 6.11). Again, non–dust particles are distinguished between smoke (black in Fig. 6.11) and marine (blue in Fig. 6.11) particle matter. These profiles show that dust mostly contributes to the total particle mass in the free troposphere on 5 May, 9 May, 14 May, and 23 May 2013 (Fig. 6.11a–c) with maximum values about 120 $\mu\text{g m}^{-3}$, 90 $\mu\text{g m}^{-3}$, 120 $\mu\text{g m}^{-3}$, and 560 $\mu\text{g m}^{-3}$, respectively. Moreover, it is noticeable that the maximum height of the dust layer decreases with transport time. Dust layer base and top heights of 0.9–2 km, 1.8–3.2 km, 1–4 km, and 0.2–4.2 km on 5 May, 9 May, 14 May, and 23 May 2013, respectively, are consistent with results from the analysis of the volume depolarization profiles as stated above. While on 9 May and 14 May the maximum mass concentration is near the dust layer base, the maximum concentrations on 5 May and 23 May are at the dust layer top and center, respectively. However,
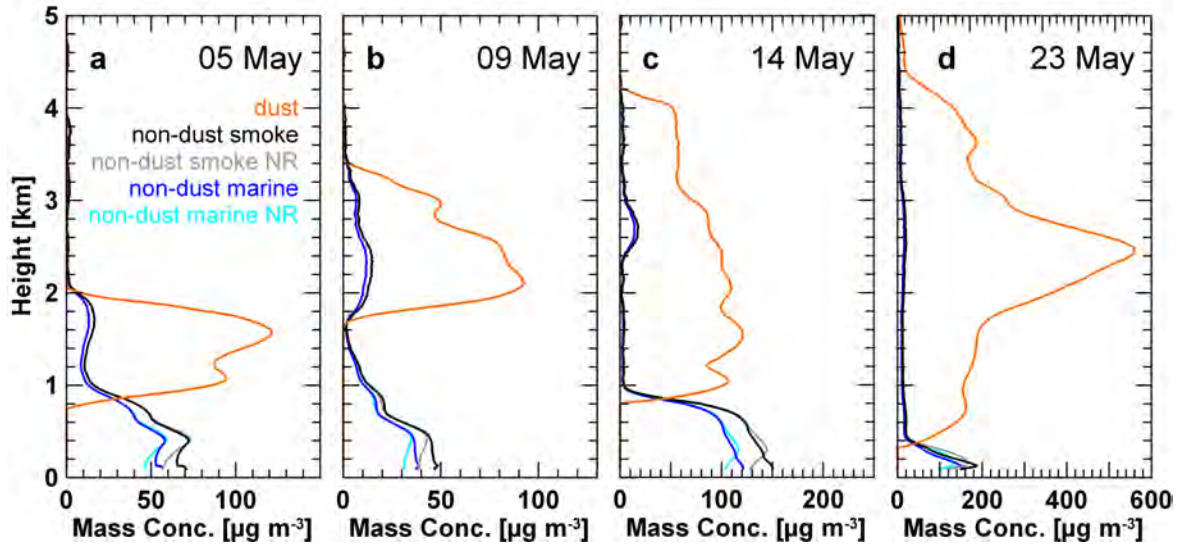

Figure 6.11: Mass concentration profiles of dust (orange) and non–dust (black and gray for smoke, blue and cyan for marine particles) aerosol particles calculated with the POLIPHON method using lidar–derived data for the periods of 05 May 2013, 2340–0035 UTC (**a**), 09 May 2013, 2315–2400 UTC (**b**), 14 May 2013, 2345–0020 UTC (**c**), and 23 May 2013, 0345–0500 UTC (**d**).

fine–mode particles prevail in the MBL on 5 May, 9 May, and 14 May 2013. As mentioned in Sect. 3.8, particles in the MBL are considered to be marine particles only. They assume maximum mass concentrations about $60\,\mu g\,m^{-3}$, $35\,\mu g\,m^{-3}$, and $115\,\mu g\,m^{-3}$, respectively, in the lowermost 1 km. As stated above (compare Fig. 6.9), on 23 May 2013 marine particles only prevailed in the lowermost part of the troposphere up to 200 m above the lidar with a maximum mass concentration of $140\,\mu g\,m^{-3}$ (Fig. 6.11d). Higher up, dust is more and more dominating. In each case study, non–dust particles in the FT show approximately the same mass concentration (12–$16\,\mu g\,m^{-3}$), disregarding whether they are considered to be smoke or marine particles. However, regarding the particle extinction coefficients of the separated aerosol types (e.g. Figure 6.10d) and corresponding total particle extinction coefficients in Fig. 6.4, fine–mode particles in the FT are most likely dominated by marine particles. This is also the fact in some of the distinct aerosol type mass concentration simulations by MACC which are discussed in Sect. 6.4. The presence of marine particles would also explain the comparatively small lidar ratios. 5 May, 9 May, and 14 May 2013 show maximum dust mass concentrations in the same size range without recognizable changes due to transport. This is in agreement with the work of *Weinzierl et al.* [2009] where surprisingly large particles were found after transport of several thousands of kilometers.

6.3 Statistical analysis

16 late evening and night measurement periods, respectively, were selected in order to apply the Raman method (see Sect. 3.5). Those data were divided into two layers containing primarily dust and marine particles, respectively (see Table 6.1). Further investigations on the aerosol particle mixture are discussed in Sect. 6.2 and 6.4. For now the two layers are named marine and dust layer, being aware also other components are present in the air masses. As stated above (see Sect. 6.2) nighttime measurements on 23 May 2013 show no indications of a MBL above 500 m (see Fig. 6.9) and are therefore not considered in the marine layer characterization in Table 6.1 (top). Deviations in base and top heights from those stated above result from the consideration of the smoothing length during averaging. Figure 6.12 gives an overview of the RV Meteor cruise measurement period in terms of the dust layer mean values (orange dots in 6.12) of the 532 nm backscatter coefficient (upper panel, 6.12a), the 532 nm extinction coefficient (6.12b), the 532 nm lidar ratio (6.12c), and the 532 nm particle depolarization ratio (6.12d). Same mean values are shown for the marine layers (blue dots in 6.12) derived from the N/R 532 nm signals. Error bars show the standard deviation influenced by retrieval uncertainties and atmospheric variability. The lower panel (6.12e) shows the column–integrated dust mass concentrations calculated with the POLIPHON method. Figure 6.12a shows mean backscatter coefficients. Results for the lofted dust layer are in good agreement with backscatter coefficients obtained between 2 and 4 km height asl during SAMUM ($\beta \approx 0.8$–$1.5\,Mm^{-1}\,sr^{-1}$, see Fig. 2.1, *Tesche et al.* [2011], *Freudenthaler et al.* [2009], *Groß et al.* [2011]) despite the observations on 23 May which show backscatter coefficients from 3.2–$3.6\,Mm^{-1}\,sr^{-1}$. Mean backscatter coefficients within the MBL range between

Table 6.1: Overview of available lidar data sets for the marine layer (top) and dust layer (bottom). High–quality signals above 0.4 km could be used. The vertical resolution is 7.5 m. Data for the marine layer are smoothed with 187.5 m and dust layer data are smoothed with 307.5 m. Height levels result after subtracting half a smoothing length at the base and top, respectively. Case studies are marked yellow.

marine layer					
Date	Time [UTC]	Base [km]	Top [km]	Thickness [km]	Height levels
02 May 2013	02:00-03:00	0.4	0.9	0.5	55
03 May 2013	00:33-01:14	0.4	1.0	0.6	68
04 May 2013	20:30-21:15	0.4	0.9	0.5	55
05 May 2013	22:15-23:15	0.4	1.0	0.6	68
05 May 2013	23:40-00:35	0.4	0.8	0.4	41
07 May 2013	01:10-01:55	0.4	1.0	0.6	68
09 May 2013	04:00-04:45	0.4	1.1	0.7	81
09 May 2013	23:15-00:00	0.4	1.4	1.0	121
10 May 2013	23:00-23:40	0.4	1.1	0.7	81
12 May 2013	00:33-00:59	0.4	1.0	0.7	68
13 May 2013	02:20-03:00	0.4	1.0	0.7	68
14 May 2013	23:45-00:20	0.4	0.8	0.4	41
17 May 2013	23:00-23:55	0.4	1.15	0.75	88
19 May 2013	03:15-04:15	0.4	1.0	0.7	68
dust layer					
Date	Time [UTC]	Base [km]	Top [km]	Thickness [km]	Height levels
05 May 2013	22:15-23:15	1.45	1.9	0.45	19
05 May 2013	23:40-00:35	1.0	2.0	1.0	92
09 May 2013	23:15-00:00	1.8	3.1	1.3	113
10 May 2013	23:00-23:40	1.7	3.0	1.3	113
12 May 2013	00:33-00:59	2.0	4.5	2.5	273
13 May 2013	02:20-03:00	1.4	4.0	2.6	286
14 May 2013	23:45-00:20	1.5	3.5	2.0	206
17 May 2013	23:00-23:55	1.55	2.9	1.35	119
19 May 2013	03:15-04:15	1.5	3.6	2.1	220
23 May 2013	00:10-01:20	0.9	4.0	3.1	352
23 May 2013	03:45-05:00	0.9	4.0	3.1	352

0.9 and $5.7 \, \mathrm{Mm^{-1} \, sr^{-1}}$.

According to AERONET typical marine optical depth is about 0.05 at 500 nm, and thus extinction coefficients from 50–$100 \, \mathrm{Mm^{-1}}$ are to be expected [*Albert Ansmann*, personal communication, June, 2015]. This is in sufficient agreement with our results for the 532 nm mean extinction coefficients within the MBL in Fig. 6.12b (blue). Mean extinction coefficients for the lofted dust layers are consistent with values from the SAMUM campaign between 2 and 4 km height asl ($\alpha \approx 48$–$97 \, \mathrm{Mm^{-1}}$, see Fig. 2.1, *Tesche et al.* [2011], *Freudenthaler et al.* [2009], *Groß et al.* [2011]). Extinction coefficients on 23 May, however, are considerably high with values of about $170 \, \mathrm{Mm^{-1}}$.

Pannel 6.12c shows the 532 nm lidar ratios. Marine layer mean values are of about 20 sr. This is in good agreement with observations during SAMUM–2b where lidar ratios of 18 sr were measured under marine conditions [*Tesche et al.*, 2011] and the study by *Müller et al.* [2007b]
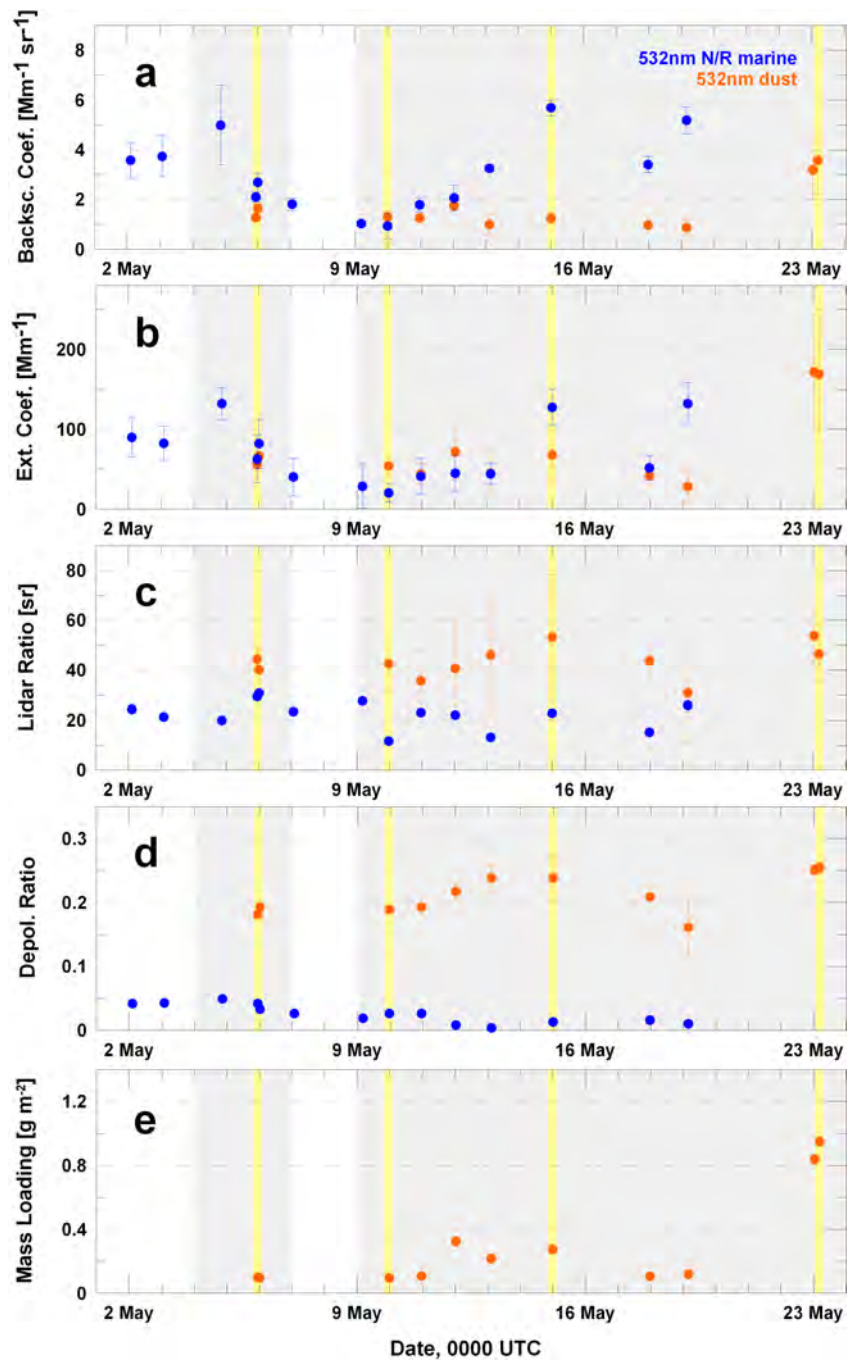
Figure 6.12: Layer mean values of 532 nm backscatter (**a**) and extinction (**b**) coefficient, lidar ratio (**c**), and particle linear depolarization ratio (**d**) for the marine (blue dots) and dust (orange dots) layers as defined in Table 6.1. Vertical bars show the standard deviations for the 14 marine and 11 dust layers. Pannel **e** shows column–integrated dust mass concentrations obtained from the POLIPHON method. Gray shades indicate dust plumes and yellow lines show dates of the case studies.

where lidar ratios of 20–26 sr were found for marine particles in the boundary layer. However, mean lidar ratios in the dust layers are around 40 sr. These values are considerably lower than preliminary findings for pure dust conditions ($S_d \approx$ 53–61 sr, see Fig. 2.1, *Tesche et al.* [2011], *Freudenthaler et al.* [2009], *Groß et al.* [2011]). As indicated in Sect. 6.2, these low lidar ratios may result from lofted marine aerosol. Marine particles are transported upward and dust particles downward by turbulent mixing processes during the long–range transport over the Atlantic. Mean lidar ratios in the lofted aerosol layers on 14–15 May and 23 May 2013, however, show values for pure dust conditions (53 sr and 54 sr, respectively).

Mean particle depolarization ratios (see 6.12d) in the marine MBL are all below 0.05 which indicate that the spherical marine particles (at relative humidities >50%, *Sakai et al.* [2010]) dominate backscattering of laser light. This result is consistent with findings of particle depolarization ratios in the MBL of 0.02±0.02 for fine-mode and wet marine particles during SAMUM–2 [*Groß et al.*, 2011]. Mean depolarization ratios in the lofted aerosol layers are around 0.2 (orange in 6.12d), i.e. less than values for pure dust conditions (0.31±0.04, *Freudenthaler et al.* [2009], *Groß et al.* [2011]). On 19 May 2013, particle depolarization ratios are even lower (0.16±0.05) which indicates the presence of a considerable amount of non–dust particles. However, the particle depolarization ratios in the lofted layers on 13 May, 14–15 May and 23 May are slightly higher with mean values of 0.24, 0.24, and 0.26, respectively. Those air masses are dominated by mineral dust aerosol.

The column–integrated mineral dust mass concentrations are shown in 6.12e. Those mass concentrations have been obtained from the POLIPHON method (see Sect. 3.8) where dust particles have been separated from non–dust particles. As can be seen, the dust mass concentrations in the period of 5–20 May 2013 show values of 0.10–0.33 g m^{-2} and comparably high mass concentrations of 0.84–0.95 g m^{-2} on 23 May 2013.

6.4 Model comparison

Desert dust models are essential to understand dust emission, transport and removal processes and predict the impact of dust on surface level particulate matter concentrations [see *http://www.bsc.es/earth-sciences/mineral-dust-forecast-system*]. Observations such as the ship–based lidar measurements, presented in the previous sections, are very important to validate dust models and to verify model simulations in detail. Here, we compare lidar observations and model simulations in terms of the mineral dust mass concentration profiles. Lidar–derived mass concentrations are calculated by means of the POLIPHON method (see Sect. 3.8). The uncertainty in the lidar–derived mass concentrations are about 30%. Figure 6.13 shows the comparison of dust mass concentration profiles computed with NMMB/BSC-Dust, SKIRON, and MACC (see Sect. 5 for model descriptions) with the lidar–derived dust mass concentration profiles for the selected case studies (shown in Fig. 6.11). There were no simulations available from NMMB/BSC-Dust for 23 May 2013.

Lidar–derived mass concentrations are the same as the ones presented in Sect. 6.2. On 5 May 2015 (Fig. 6.13a), a lofted mineral dust aerosol layer was observed in the height range from 0.9–2.0 km with a column–integrated mass concentration of $0.10\,\mathrm{g\,m^{-2}}$. The same integrated mass concentration was obtained from SKIRON simulations. However, the dust layer was simulated between 0.2–3.0 km with a maximum of $90\,\mathrm{\mu g\,m^{-3}}$ around 1 km height. According to the lidar observations, the dust layer center was about 500 m higher. NMMB/BSC-Dust results shows a comparably high column–integrated mass concentration of $0.23\,\mathrm{g\,m^{-2}}$. Dust
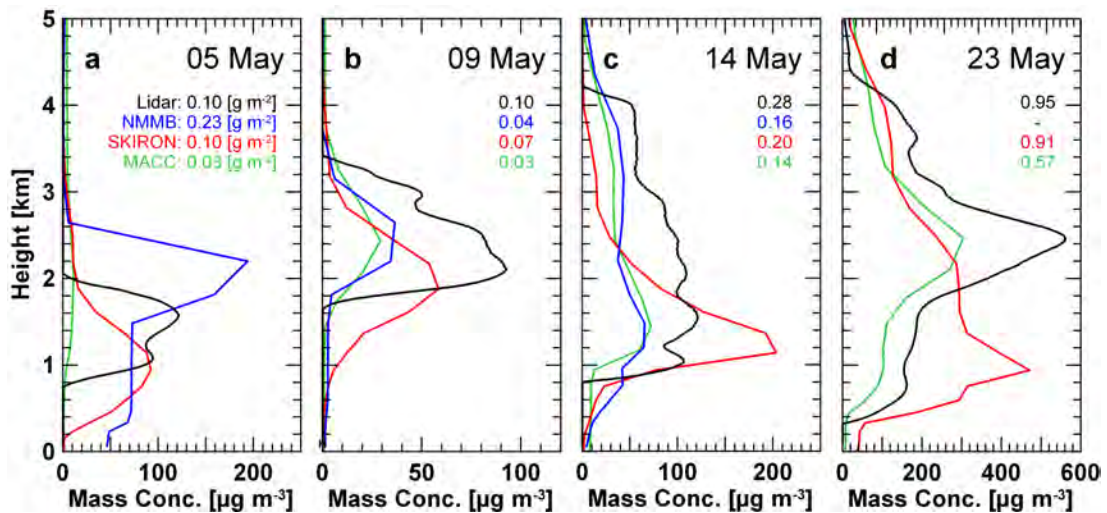
Figure 6.13: Averaged mass concentration profiles for the periods of 05 May 2013 2340 UTC to 0035 UTC (**a**), 09 May 2013 2315 to 2400 UTC (**b**), 14 May 2013 2345 to 0020 UTC (**c**), and 23 May 2013 0345 to 0500 UTC (**d**). Lidar–derived findings (black) are compared to model results of NMMB/BSC-Dust (blue), SKIRON (red), and MACC (green).

particles are also simulated throughout the MBL with mass concentrations up to $70\,\mu\mathrm{g\,m^{-3}}$. The dust maximum is at 2.2 km, and thus 700 m above the observed dust layer center height. MACC simulations show little dust aerosol at all with column–integrated mass concentration of $0.03\,\mathrm{g\,m^{-2}}$. The dust layer was at the heights from 1.0–3.0 km after the MACC model. The 5 May comparison is the most difficult one, because the dusty air masses traveled more than 10 days from the Saharan regions to the western part of the tropical Atlantic.

Lidar–derived mass concentrations on 9 May 2013 show the same total column–integrated mass concentration as on 5 May (Fig. 6.13b). The dust layer was observed between 1.8–3.2 km height with a maximum dust concentration of $90\,\mu\mathrm{g\,m^{-3}}$ at 2 km height. The aerosol layer on 9 May is well depicted by the NMMB/BSC-Dust and MACC models. Again, SKIRON simulations show a lowered aerosol layer in the height range from 1.0–3.2 km. Regarding the column–integrated mass concentration, SKIRON shows results closest to the lidar–derived findings with $0.07\,\mathrm{g\,m^{-2}}$. The remaining models show values of 0.03–$0.04\,\mathrm{g\,m^{-2}}$ only. Dust emission seems to be underestimated by NMMB/BSC-Dust and MACC whereas sedimentation speed seems to be too high in the case of SKIRON.

Figure 6.13c shows mass concentration profiles on the 14 May 2013. The dust layer was observed in the height range from 1–4 km. The column–integrated mass concentration was $0.28\,\mathrm{g\,m^{-2}}$. The behavior of lidar–derived mass concentration profile is well depicted by NNB/BSC-Dust and MACC but both show almost half the column–integrated mass concentration compared to the lidar–derived profile with values of $0.16\,\mathrm{g\,m^{-2}}$ and $0.14\,\mathrm{g\,m^{-2}}$, respectively. The SKIRON simulation indicates dust in the same height range. However, compared to the other results, the mass concentration shows a strong maximum around 1.2 km asl (with $200\,\mu\mathrm{g\,m^{-3}}$ almost a factor of 2 higher than the maximum of the lidar measurement) and decreases rapidly with height. The column–integrated mass concentration of $0.20\,\mathrm{g\,m^{-2}}$ is, however, close to the lidar findings.

Dust mass concentration simulations on 23 May 2013 were performed by SKIRON and MACC. The lidar–derived dust mass profile in the height range between 0.2–4.2 km shows a strong maximum at 2.5 km height with a value of almost $600\,\mu\mathrm{g\,m^{-3}}$. The MACC profile again well depicts this dust layer. It has its maximum in the same height range. Again the mass loading is underestimated. The column–integrated mass concentration is only $0.57\,\mathrm{g\,m^{-2}}$ instead of the observed value of $0.95\,\mathrm{g\,m^{-2}}$. The column–integrated mass concentration obtained with SKIRON is similar to the lidar value $(0.91\,\mathrm{g\,m^{-2}})$. The SKIRON dust mass profile also shows a strong maximum of almost $500\,\mu\mathrm{g\,m^{-3}}$, but at considerably lower height. A wrong dust particle sedimentation parametrization seems to be the reason for the deviations from the observations.

All in all, it is visible that SKIRON shows the aerosol layers at lower heights in all cases compared to the lidar findings but consistent results in terms of column–integrated mass concentrations. This may result from an insufficient buoyancy parametrization as mentioned. MACC results seem to be less consistent with the lidar findings in terms of the total dust amount the longer the air masses have been transported. This may be due to a wrong dust emission or deposition scheme. The NNB/BSC-Dust model column integrated mass

concentration differs from the lidar values by the factor 2 (overestimation on 05 May, underestimation on 09 and 14 May). Furthermore, it is visible that lidar findings mainly show the highest column–integrated mass concentrations.

Mass concentration profiles have been calculated for distinct aerosol types by MACC for the same case studies (Fig. 6.14a–d). Dust mass concentrations (solid orange lines in Fig. 6.14) are the same as MACC results shown in Fig. 6.13 (green lines). In addition to that, mass concentration profiles for marine particles (solid blue lines in Fig. 6.14) and black carbon particles (solid black lines in Fig. 6.14) simulated with MACC are shown. The latter is known as a tracer for biomass–burning smoke. Its mass fraction in smoke can be as high as 5% [*Saide et al.*, 2015; *Haywood et al.*, 2003; *Abel et al.*, 2003]. The black carbon mass concentration is thus multiplied by the factor 20 in Fig. 6.14 to roughly represent the mass concentration of biomass–burning smoke and can be interpreted as an indication for the presence of smoke in the lofted dust plume. Figure 6.14 also shows the lidar–derived mass concentration profiles for dust (dashed orange lines), marine particles (dashed blue lines) and smoke particles above the MBL (dashed black lines) which have been already discussed in Sect. 6.2. In contrast to the MACC results, the aerosol separation based on lidar data distinguishes between dust and non–dust aerosols only. For the resulting mass concentration profiles (see Fig. 6.11) we may assume that the non–dust particles are either smoke or marine particles. The analysis in Sect. 6.2 indicates that the non–dust particles are most probably marine particles. Differences in the dust mass concentration have been discussed above (see Fig. 6.13, black
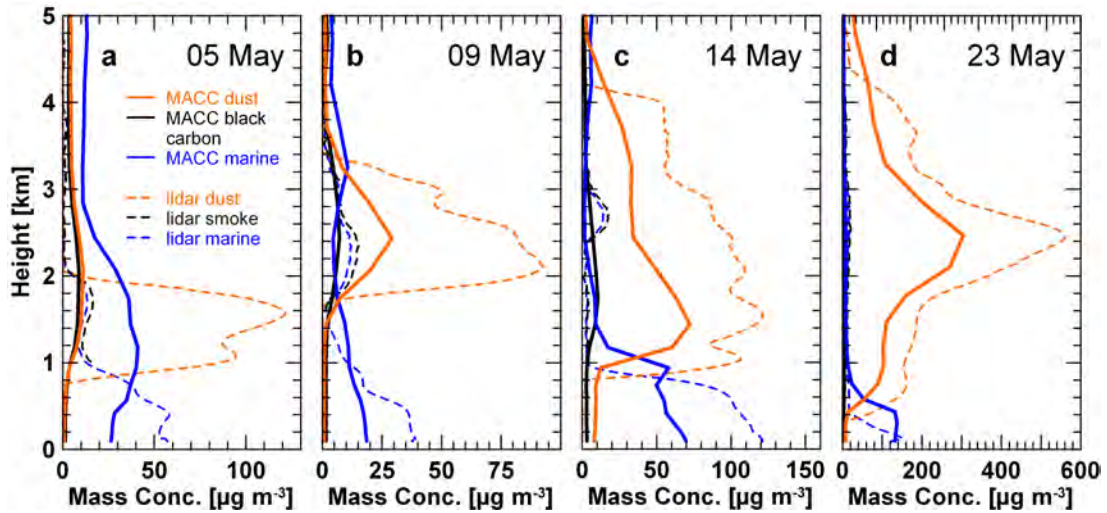
Figure 6.14: Mass concentration profiles of sea salt (solid blue lines), black carbon ×20 (solid black lines), and mineral dust (solid orange lines) aerosol particles from MACC simulations. 3–h averages are shown for 05 May 2013, 2400 UTC (**a**), 09 May 2013, 2400 UTC (**b**), 14 May 2013, 2400 UTC (**c**), and 23 May 2013, 0300 UTC (**d**). Those profiles are compared to the lidar–derived mass concentration profiles of sea salt (dashed blue lines), smoke (dashed black lines above the MBL only), and mineral dust (dashed orange lines) particles.

and green lines). MACC indicates that marine particles dominate the whole profile on 5 May 2013 with a maximum of 40 μg m^{-3} at 1 km height. Values of about 10–15 μg m^{-3} were simulated for heights >3 km. In comparison to that, the lidar findings show a well defined MBL top of 1 km asl and maximum values of about 60 μg m^{-3} at 400 m asl.

MACC profiles on 9 May 2013 show that marine aerosol is present throughout the whole layer. The maximum of the marine mass concentration is at sea level (20 μg m^{-3}), decreasing up to 2.4 km (5 μg m^{-3}) where the maximum dust mass concentration is modeled. There is a second maximum of marine particles at 3.3 km (10 μg m^{-3}). The lidar–derived sea–salt mass concentration profile (blue in Fig. 6.11b) shows a similar behavior with maximum values almost a factor of 2 higher than the maximum of the MACC simulation. The marine particle mass concentration minimum of lidar measurements is at 1.6 km height.

Marine particle mass concentration calculated by MACC on 14 May 2013 again underestimate the maximum value at sea level (MACC: 70 μg m^{-3}, lidar: 120 μg m^{-3}). The MBL is simulated at 1 km asl. For heights above the MBL the marine particle mass concentration shows values <10 μg m^{-3}. Lidar–derived findings shows the MBL top height at 800 m asl and a second maximum of 15 μg m^{-3} from 2.5–3.0 km. On 23 May 2013, both MACC and Lidar results for marine particle mass concentration are consistent with maximum values of about 140 μg m^{-3} throughout the MBL. The MBL top heights are simulated at 500 m and measured at 350 m by lidar. Smoke mass concentration profiles above the MBL obtained from the POLIPHON method are also plotted in Fig. 6.14 (dashed black lines), although previous results showed that marine particles most probably dominate the non–dust mass concentration fraction in the FT. As stated above, the simulated MACC black carbon mass concentration times 20 (solid black lines in Fig. 6.14) is a rough estimate for the smoke amount. MACC shows that traces smoke were present. Smoke layers are indicated from 1–3 km, 1.5–3.5 km and 1–3 km on 5, 9, and 14 May respectively. All show maximum values of about 15 μg m^{-3}. As pointed out in Sect. 6.2, marine particles most probably dominate the non–dust mast fraction in the FT. However, smoke layers calculated with the POLIPHON method are in the same height range and differ only slightly from the maximum and total smoke mass concentration.

In summary, it can be stated that MACC shows that marine aerosol particles can reach heights up to 3–4 km which is in reasonable agreement with the lidar observation, although the lidar–derived mass concentrations of marine particles in the FT are considerably lower. MBL top heights calculated by MACC are generally higher than top heights observed by lidar. MACC marine mass concentration maximum values in the MBL, however, are mainly smaller than the lidar–derived maximum values. Those facts indicate an overestimated buoyancy in the MBL and mixing processes in the FT.

Chapter 7

Summary and conclusion

This work showed the analysis of air masses over the North Atlantic Ocean by means of lidar measurements during the RV Meteor cruise in spring 2013. The main goal was the characterization of the Saharan air layer along its transport route from North Africa towards the Caribbean to investigate possible aging effects of mineral dust aerosol particles. Furthermore, a model comparison was performed in order to validate aerosol transport model in terms of the dust emission, transport, and deposition. The data were obtained from Polly^{XT} lidar measurements and a microtops II sun–photometer, which was operated by the Maritime Aerosol Network. Both instruments were mounted aboard the RV Meteor during the cruise from 29 April to 23 May 2013 from Guadeloupe towards Cape Verde. Underlying mathematical concepts and equations, physical processes, measurement instruments, aerosol transport models, and an overview of previous findings were presented.

Polly^{XT} is a multiwavelength Raman and polarization lidar. Together with launched regularly soundings, profiles of the optical properties in terms of the backscatter and extinction coefficient, lidar ratio, Ångström exponent, and particle linear depolarization ratio could be computed for 16 measurement sequences between 5–23 May 2013. Mean values in the MBL and lofted aerosol layers were presented. As the first step, the observations on 5 May, 9 May, 14 May, and 23 May 2013 were discussed in detail. HYSPLIT–backward trajectories indicated that the last three of these four observations characterize an almost fresh dust layer, whereas the observation around 5 May showed an aged dust layer with almost 10 days of travel over the ocean. Constant depolarization ratios and wavelength–independent extinction coefficients indicated well–mixed layers. Whereas lidar ratios and particle depolarization ratios on 5 and 9 May were considerably low with values about 40–53 sr and 20%, respectively, the cases of 14 and 23 May showed values of 47–66 sr and 26–27% which are in reasonable agreement with results from SAMUM for pure dust ($S_\mathrm{d} \approx 53$–$61\,\mathrm{sr}$, $\delta_\mathrm{d} \approx 26$–$37\%$, *Tesche et al.* [2011], *Freudenthaler et al.* [2009], *Groß et al.* [2011]).

Measurements from the AERONET–MAN microtops II sun photometer provided additional aerosol optical thickness (AOT) and Ångström exponent data. For the aged dust plume from 4–6 May 2013 an AOT of 0.5 and Ångström exponent of 0.3 were measured. The observed dust plume in the period from 9–23 May 2013 showed an AOT of 0.28 and Ångström

exponent of 0.2.

As the next step, we used the POLIPHON algorithm, which enables the separation of distinct aerosol types, to compute the profiles of dust and non–dust mass concentrations for these four cases. These profiles showed maximum dust mass concentrations of $120\,\mu\mathrm{g\,m^{-3}}$, $90\,\mu\mathrm{g\,m^{-3}}$, $120\,\mu\mathrm{g\,m^{-3}}$, and $560\,\mu\mathrm{g\,m^{-3}}$ on 5 May, 9 May, 14 May, and 23 May 2013, respectively. Contrary to our expectations, the POLIPHON method application showed that the smoke amount in the FT was small. By comparison of particle and total extinction coefficients we found that marine particles most probably dominate the non–dust mass fraction throughout the aerosol layers. This is in reasonable agreement with the low lidar ratios observed in the cases.

As the final step, mineral dust mass concentrations simulated with the models MACC, NMMB/BSC–Dust, and SKIRON have been compared to the lidar–derived dust mass concentration results. The column–integrated mass concentration showed that the dust mass loading is generally underestimated in all models. It is also visible that the vertical distribution often differs from the lidar–derived profiles. Moreover, MACC provided mass concentration profiles of marine and black carbon particles which were compared to the non–dust mass concentration profiles from lidar measurements. MACC shows high mineral particle mass concentrations in the FT up to 3–4 km height. Furthermore, simulated MBL top heights are around 400 m higher than top heights observed by lidar.

All in all, significant differences in the dust optical properties in the discussed two dust plumes were found and may result from aging effects. The model comparison showed that further improvements in aerosol transport models are required to adequately describe dust load and vertical distribution. A model comparisons with COSMO–MUSCAT will soon be included in the aerosol model validation. For the first time, data of the optical properties of Saharan air masses were collected along the transport over the North Atlantic Ocean towards the Caribbean. Those data will be integrated in the SAMUM (Saharan Mineral Dust Experiment) and SALTRACE (Saharan Aerosol Long-range Transport and Aerosol-Cloud-Interaction Experiment) projects. They will link the retrieved data near the mineral dust source and data in the receptor region after the long–range transport.

Bibliography

Abel, S. J., J. M. Haywood, E. J. Highwood, J. Li, and P. R. Buseck (2003), Evolution of biomass burning aerosol properties from an agricultural fire in southern africa, *Geophysical Research Letters*, *30*(15), 1783, doi:10.1029/2003GL017342.

Althausen, D., R. Engelmann, H. Baars, B. Heese, A. Ansmann, D. Müller, and M. Komppula (2009), Portable Raman lidar Polly^{XT} for automated profiling of aerosol backscatter, extinction, and depolarization, *Journal of Atmospheric and Oceanic Technology*, *26*, 2366–2378, doi:10.1175/2009JTECHA1304.1.

Ångström, A. (1964), The parameters of atmospheric turbidity, *Tellus*, *16*, 64–75.

Ansmann, A., and D. Müller (2005), *Lidar - Range-Resolved Optical Remote Sensing of the Atmosphere*, vol. 102, chap. Lidar and Atmospheric Aerosol Particles, pp. 105–141, C. Weitkamp, Springer Berlin/Heidelberg.

Ansmann, A., M. Riebesell, and C. Weitkamp (1990), Measurement of atmospheric aerosol extinction profiles with a Raman lidar, *Opt. Lett.*, *15*, 746–748.

Ansmann, A., U. Wandinger, M. Riebesell, C. Weitkamp, and W. Michaelis (1992), Independent measurement of extinction and backscatter profiles in cirrus clouds by using a combined Raman elastic–backscatter lidar, *Applied Optics*, *31*, 7113–7131.

Ansmann, A., M. Tesche, P. Seifert, D. Althausen, R. Engelmann, J. Fruntke, U. Wandinger, I. Mattis, and D. Müller (2009), Evolution of the ice phase in tropical altocumulus: SAMUM lidar observations over Cape Verde, *Journal of Geophysical Research*, *114*, D17208, doi:10.1029/2008JD011659.

Ansmann, A., M. Tesche, P. Seifert, S. Groß, V. Freudenthaler, A. Apituley, K. M. Wilson, I. Serikov, H. Linné, B. Heinold, A. Hiebsch, F. Schnell, J. Schmidt, I. Mattis, U. Wandinger, and M. Wiegner (2011), Ash and fine-mode particle mass profiles from EARLINET-AERONET observations over central Europe after the eruptions of the Eyjafjallajökull volcano in 2010, *Journal of Geophysical Research: Atmospheres*, *116*(D20), doi:10.1029/2010JD015567, D00U02.

Ansmann, A., P. Seifert, M. Tesche, and U. Wandinger (2012), Profiling of fine and coarse particle mass: Case studies of Saharan dust and Eyjafjallajökull/Grimsvötn volcanic plumes, *Atmos. Chem. and Phys.*, *12*, 9399–9415, doi:10.5194/acp-12-9399-2012.

Ansmann, A., D. Althausen, T. Kanitz, R. Engelmann, A. Skupin, H. Baars, A. Klepel, M. Haarig, B. Heinold, I. Tegen, C. Toledano, D. Prescod, and D. Farrell (2014), Saharan dust long–range transport: SALTRACE lidar observations at Barbados and aboard RV Meteor (Guadaloupe to Cape Verde) versus dust transport modelling, Proceedings, DUST 2014 – International Conference on Atmospheric Dust, Castellaneta, Italy, 1–6 June 2014.

Balkanski, Y., M. Schulz, T. Claquin, and S. Guibert (2007), Reevaluation of Mineral aerosol radiative forcings suggests a better agreement with satellite and AERONET data, *Atmospheric Chemistry and Physics*, *7*(1), 81–95, doi:10.5194/acp-7-81-2007.

Bauer, S. E., Y. Balkanski, M. Schulz, D. A. Hauglustaine, and F. Dentener (2004), Global modeling of heterogeneous chemistry on mineral aerosol surfaces: Influence on tropospheric ozone chemistry and comparison to observations, *Journal of Geophysical Research*, *109*, doi:10.1029/2003JD003868, D02304.

Betts, A. K. (1986), A new convective adjustment scheme. Part I: Observational and theoretical basis, *Quarterly Journal of the Royal Meteorological Society*, *112*(473), 677–691, doi:10.1002/qj.49711247307.

Betts, A. K., and M. J. Miller (1986), A new convective adjustment scheme. Part II: Single column tests using GATE wave, BOMEX, ATEX and arctic air-mass data sets, *Quarterly Journal of the Royal Meteorological Society*, *112*(473), 693–709, doi:10.1002/qj.49711247308.

Böckmann, C. (2001), Hybrid regularization method for the ill-posed inversion of multiwavelength lidar data in the retrieval of aerosol size distributions, *Appied Optics*, *40*, 1329–1342.

Carlson, T. N., and J. M. Prospero (1972), The Large-Scale Movement of Saharan Air Outbreaks over the Northern Equatorial Atlantic, *J. Appl. Meteor.*, *11*, 283–297.

Chen, Y.-L. (1985), Tropical squall lines over the eastern Atlantic during GATE, *Mon. Weather Rev.*, *113*, 2015–2022.

Dubovik, O., A. Sinyuk, T. Lapyonok, B. N. Holben, M. Mishchenko, P. Yang, T. F. Eck, H. Volten, O. Muñoz, B. Veihelmann, W. J. van der Zande, J.-F. Leon, M. Sorokin, and I. Slutsker (2006), Application of spheroid models to account for aerosol particle nonsphericity in remote sensing of desert dust, *Journal of Geophysical Research: Atmospheres*, *111*(D11), doi:10.1029/2005JD006619, D11208.

Dunion, J. P., and C. S. Velden (2004), The Impact of the Saharan Air Layer on Atlantic Tropical Cyclone Activity, *Bull. Amer. Meteor. Soc.*, *85*, 353–365.

Engelmann, R., T. Kanitz, H. Baars, B. Heese, D. Althausen, A. Skupin, U. Wandinger, M. Komppula, I. S. Stachlewska, V. Amiridis, E. Marinou, I. Mattis, H. Linné, and A. Ansmann (2015), EARLINET Raman Lidar Polly^{XT}: the neXT generation, *Atmos. Meas. Tech. Discuss.*, *8*, 1–44, doi:10.5194/amtd-8-1-2015.

Fécan, F., B. Marticorena, and G. Bergametti (1999), Parametrization of the increase of the aeolian erosion threshold wind friction velocity due to soil moisture for arid and semi-arid areas, *Annales Geophysicae*, *17*(1), 149–157, doi:10.1007/s00585-999-0149-7.

Fernald, F. G. (1984), Analysis of atmospheric lidar observations: some comments, *Applied Optics*, *23*, 652–653.

Ferrier, B. S., Y. Jin, Y. Lin, T. Black, E. Rogers, and G. DiMego (2002), Implementation of a new grid-scale cloud and precipitation scheme in the NCEP Eta Model, Proc. 15th Conf. on Numerical Weather Prediction, 12–16 August 2002, San Antonio, TX, Amer. Meteor. Soc., pp. 280–283.

Freudenthaler, V., M. Esselborn, M. Wiegner, B. Heese, M. Tesche, A. Ansmann, D. Müller, D. Althausen, M. Wirth, A. Fix, G. Ehret, P. Knippertz, C. Toledano, J. Gasteiger, M. Garhammer, and M. Seefeldner (2009), Depolarization ratio profiling at several wavelengths in pure Saharan dust during SAMUM 2006, *Tellus Series B*, *61*(1), 165–179, doi:10.1111/j.1600-0889.2008.00396.x.

Ginoux, P., M. Chin, I. Tegen, J. M. Prospero, B. Holben, O. Dubovik, and S.-J. Lin (2001), Sources and distributions of dust aerosols simulated with the GOCART model, *Journal of Geophysical Research: Atmospheres*, *106*(D17), 20255–20273, doi:10.1029/2000JD000053.

Groß, S., M. Tesche, V. Freudenthaler, C. Toledano, M. Wiegner, A. Ansmann, D. Althausen, and M. Seefeldner (2011), Characterization of Saharan dust, marine aerosols and mixtures of biomass-burning aerosols and dust by means of multi-wavelength depolarization and Raman lidar measurements during SAMUM 2, *Tellus Series B*, *63*(4), 706–724, doi:10.1111/j.1600-0889.2011.00556.x.

Haywood, J. M., S. R. Osborne, P. N. Francis, A. Keil, P. Formenti, M. O. Andreae, and P. H. Kaye (2003), The mean physical and optical properties of regional haze dominated by biomass burning aerosol measured from the C-130 aircraft during SAFARI 2000, *Journal of Geophysical Research: Atmospheres*, *108*(D13), doi:10.1029/2002JD002226, 8473.

Heinold, B., I. Tegen, S. Bauer, and M. Wendisch (2011), Regional modelling of Saharan dust and biomass burning smoke Part 2: Direct radiative forcing and atmospheric., *Tellus Series B*, *63(4 (Special Issue))*, 800–813, doi:10.1111/j.1600-0889.2011.00574.x.

IPCC (Ed.) (2007), *Climate Change 2007: The Scientific Basis. Contribution of Working Group I to the Fourth Assessment Report of the Intergovernmental Panel on Climate Change*, 996 pp., Cambridge University Press, Solomon, S., Qin, D., Manning, M., Chen, Z., Marquis, M., Averyt, K. B., Tignor, M. and Miller, H. L.

Janjic, Z., H. Huang, and S. Lu (2009), A unified atmospheric model suitable for studying transport of mineral aerosols from meso to global scales, *IOP Conference Series: Earth and Environmental Science*, *7*(1), 012011.

Janjic, Z. I. (1990), The Step-Mountain Coordinate: Physical Package, *Mon. Weather Rev.*, *118*, 1429–1443.

Janjic, Z. I. (1994), The Step-Mountain Coordinate: Further Developments of the Convection, Viscous Sublayer, and Turbulence Closure Schemes, *Amer. Meteor. Soc.*, *122*, 927–945.

Janjic, Z. I. (1997), *Research Activities in Atmospheric and Ocean Modeling*, chap. Advection scheme for passive substances in the NCEP Ete Model, (WMO, Geneva, CAS/WGNE).

Jickells, T. D., Z. S. An, K. K. Andersen, A. R. Baker, G. Bergametti, N. Brooks, J. J. Cao, P. W. Boyd, R. A. Duce, K. A. Hunter, H. Kawahata, N. Kubilay, J. LaRoche, P. S. Liss, N. Mahowald, J. M. Prospero, A. J. Ridgwell, I. Tegen, and R. Torres (2005), Global iron connections between desert dust, ocean biogeochemistry, and climate, *Science*, *308*, 67–71.

Jung, E., B. Albrecht, J. M. Prospero, H. H. Jonsson, and S. M. Kreidenweis (2013), Vertical structure of aerosols, temperature, and moisture associated with an intense African dust event observed over the eastern Caribbean, *Journal of Geophysical Research: Atmospheres*, *118*(10), 4623–4643, doi:10.1002/jgrd.50352.

Kallos, G., S. Nickovic, A. Papadopoulos, D. Jovic, O. Kakaliagou, N. Misirlis, L. Boukas, N. Mimikou, G. Sakellaridis, J. Papageorgiou, E. Anadranistakis, and M. Manousakis (1997), The Regional Weather Forecasting System SKIRON and its capability for forecasting dust uptake and transport, Proc. Of the WMO conference on dust storms, 1-6 November 1997, Damascus, Syria, 9 pp.

Kallos, G., A. Papadopoulos, P. Katsafados, and S. Nickovic (2006), Trans-Atlantic Saharan dust transport: Model simulation and results., *Journal of Geophysical Research*, *111*, doi: 10.1029/2005JD006207.

Kandler, K., L. Schütz, C. Deutscher, M. Ebert, H. Hofmann, S. Jäckel, R. Jaenicke, P. Knippertz, K. Lieke, A. Massling, A. Petzold, A. Schladitz, B. Weinzierl, A. Wiedensohler, S. Zorn, and S. Weinbruch (2009), Size distribution, mass concentration, chemical and mineralogical composition and derived optical parameters of the boundary layer aerosol at Tinfou, Morocco, during SAMUM 2006, *Tellus Series B*, *61*(1), 32–50, doi: 10.1111/j.1600-0889.2008.00385.x.

Kandler, K., K. Lieke, N. Benker, C. Emmel, M. Küpper, D. Müller-Ebert, M. Ebert, D. Scheuvens, A. Schladitz, L. Schütz, and S. Weinbruch (2011), Electron microscopy of particles collected at Praia, Cape Verde, during the Saharan Mineral Dust Experiment: particle chemistry, shape, mixing state and complex refractive index, *Tellus Series B*, *63*(4), 475–496, doi:{10.1111/j.1600-0889.2011.00550.x}.

Kanitz, T., A. Ansmann, R. Engelmann, and D. Althausen (2013), North-south cross sections of the vertical aerosol distribution over the Atlantic Ocean from multiwavelength Raman/polarization lidar during Polarstern cruises, *Journal of Geophysical Research: Atmospheres*, *118*(6), 2643–2655, doi:10.1002/jgrd.50273.

Kanitz, T., R. Engelmann, Heinold, B., H. Baars, A. Skupin, and A. Ansmann (2014), Tracking the Saharan Air Layer with shipborne lidar across the tropical Atlantic, *Geophysical Research Letters*, *41*, 1044–1050, doi:10.1002/2013GL058780.

Klett, J. (1981), Stable analytical inversion solution for processing lidar returns, *Applied Optics*, *20*, 211–220.

Koren, I., Y. J. Kaufman, L. A. Remer, and J. V. Martins (2006), The Bodélé depression: a single spot in the Sahara that provides most of the mineral dust to the Amazon forest, *Environmental Research Letters*, *1*(1), 5 pp., doi:10.1088/1748-9326/1/1/014005.

Laurent, B., B. Heinold, I. Tegen, C. Bouet, and G. Cautenet (2008), Surface wind accuracy for modeling mineral dust emissions: Comparing two regional models in a Bodélé case study, *Geophysical Research Letters*, *35*, L09804, doi:10.1029/2008GL033654.

Mamouri, R. E., and A. Ansmann (2014), Fine and coarse dust separation with polarization lidar, *Atmospheric Measurement Techniques*, *7*, 3717–3735, doi:10.5194/amt-7-3717-2014.

Marticorena, B., and G. Bergametti (1995), Modeling the atmospheric dust cycle: 1. Design of a soil-derived dust emission scheme, *Journal of Geophysical Research: Atmospheres*, *100*(D8), 16415–16430, doi:10.1029/95JD00690.

Marticorena, B., G. Bergametti, B. Aumont, Y. Callot, C. NŠDoume, and M. Legrand (1997), Modeling the Saharan dust cycle: 2. Simulation of Saharan dust sources, *Journal of Geophysical Research*, *102*, 4387–440.

Mesinger, F. (1997), Dynamics of limited-area models: formulation and numerical methods., *Meteorol. Atmos. Phys.*, *63*, 3–14.

Mesinger, F., Z. I. Janjic, S. Nickovic, and D. Gavrilov (1988), The Step-Mountain Coordinate: Model Description and Performance for Cases of Alpine Lee Cyclogenesis and for Case of an Appalachian Redevelopment, *Amer. Meteor. Soc.*, *116*, 1493–1518.

Mie, G. (1908), Beiträge zur Optik trüber Medien, speziell kolloidaler Metallösungen, *Ann. der Physik*, *25*, 337–455.

Mlawer, E. J., S. J. Taubman, P. D. Brown, M. J. Iacono, and S. A. Clough (1997), Radiative transfer for inhomogeneous atmospheres: RRTM, a validated correlated-k model for the longwave, *Journal of Geophysical Research: Atmospheres*, *102*(D14), 16663–16682, doi:10.1029/97JD00237.

Moulin, C., C. E. Lambert, F. Dulac, and U. Dayan (1997), Control of atmospheric export of dust from North Africa by the North Atlantic Oscillation, *Nature*, *387*, doi:10.1038/42679.

Müller, D., A. Ansmann, I. Mattis, M. Tesche, U. Wandinger, D. Althausen, and G. Pisani (2007a), Aerosol-type-dependent lidar ratios observed with Raman lidar, *Journal of Geophysical Research: Atmospheres*, *112*(D16), doi:10.1029/2006JD008292, D16202.

Müller, D., I. Mattis, A. Ansmann, U. Wandinger, and D. Althausen (2007b), *Advanced Environmental Monitoring*, chap. Raman lidar for monitoring of aerosol pollution in the free troposphere, pp. 155–166, Springer.

Nickovic, S., and S. Dobricic (1996), A model for long-range transport of desert dust, *Mon. Weather Rev.*, pp. 2537–2544.

Nickovic, S., G. Kallos, A. Papadopoulos, and O. Kakaliagou (2001), A model for prediction of desert dust cycle in the atmosphere, *Journal of Geophysical Research: Atmospheres*, *106*(D16), 18113–18129, doi:10.1029/2000JD900794.

Nisantzi, A., R. E. Mamouri, A. Ansmann, G. L. Schuster, and D. G. Hadjimitsis (2015), Middle East versus Saharan dust extinction-to-backscatter ratios, *Atmospheric Chemistry and Physics*, *15*(12), 7071–7084, doi:10.5194/acp-15-7071-2015.

Pérez, C., S. Nickovic, J. Baldasano, M. Sicard, F. Rocadenbosh, and V. Cachorro (2006), A long Saharan dust event over the western Mediterranean: Lidar, sun photometer observations and regional dust modeling, *Journal of Geophysical Research*, *111*, D15214, doi:10.1029/2005JD006579.

Pérez, C., K. Haustein, Z. Janjic, O. Jorba, N. Huneeus, J. M. Baldasano, T. Black, S. Basart, S. Nickovic, R. L. Miller, J. P. Perlwitz, M. Schulz, and M. Thomson (2011), Atmospheric dust modeling from meso to global scales with the online NMMB/BSC-Dust model – Part 1: Model description, annual simulations and evaluation, *Atmospheric Chemistry and Physics*, *11*(24), 13001–13027, doi:10.5194/acp-11-13001-2011.

Prather, K. A., C. D. Hatch, and V. H. Grassian (2008), Analysis of atmospheric aerosols, *Annu. Rev. Anal. Chem.*, *1*, 485–514.

Prospero, J. M., and T. N. Carlson (1972), Vertical and areal distribution of Saharan dust over the western equatorial north Atlantic Ocean, *Journal of Geophysical Research*, *77*(27), 5255–5265, doi:10.1029/JC077i027p05255.

Rodriguez, S., X. Querol, A. Alastues, G. Kallos, and O. Kakaliagou (2001), Saharan dust contribution to PM10 and TSP levels in southern and eastern Spain., *Atmos. Environ.*, *35*, 2433–2447.

Romero, O. E., C. B. Lange, R. Swap, and G. Wefer (1999), Eolian-transported freshwater diatoms and phytoliths across the equatorial Atlantic record: Temporal changes in Saharan

dust transport patterns, *Journal of Geophysical Research: Oceans, 104*(C2), 3211–3222, doi:10.1029/1998JC900070.

Saide, P. E., S. N. Spak, R. B. Pierce, J. A. Otkin, T. K. Schaack, A. K. Heidinger, A. M. da Silva, M. Kacenelenbogen, J. Redemann, and G. R. Carmichael (2015), Central American biomass burning smoke can increase tornado severity in the U.S., *Geophysical Research Letters, 42*(3), 956–965, doi:10.1002/2014GL062826.

Sakai, T., T. Nagai, Y. Zaizen, and Y. Mano (2010), Backscatterin linear depolarization ratio measurements of mineral, sea-salt, and ammonium sulfate particles simulated in a laboratory chamber, *Applied Optics, 49*, 4441–4449.

Scheuvens, D., and K. Kandler (2014), *Mineral Dust: A Key Player in the Earth System*, chap. On Composition, Morphology, and Size Distribution of Airborne Mineral Dust, pp. 15–50, Springer.

Seifert, P., A. Ansmann, I. Mattis, U. Wandinger, M. Tesche, R. Engelmann, D. Müller, C. Pérez, and K. Haustein (2010), Saharan dust and heterogeneous ice formation: Eleven years of cloud observations at a central European EARLINET site, *Journal of Geophysical Research: Atmospheres, 115*(D20), 2156–2202, doi:10.1029/2009JD013222, D20201.

Seinfeld, J. H., and S. N. Pandis (1998), *Atmospheric Chemestry and Physics: From Air Pollution to Climate Change*, New York: Wiley-Interscience, ISBN 0471178160.

Shao, Y. (2001), A model for mineral dust emission, *Journal of Geophysical Research: Atmospheres, 106*(D17), 20239–20254, doi:10.1029/2001JD900171.

Shao, Y. (2008), *Physics and Modelling of Wind Erosion*, 2nd ed., Springer.

Slinn, S. A., and W. G. N. Slinn (1980), Predictions for particle deposition on natural waters, *Atmospheric Environment, 14*, 1013–1016.

Smirnov, A., B. N. Holben, I. Slutsker, D. M. Giles, C. R. McClain, T. F. Eck, S. M. Sakerin, A. Macke, P. Croot, G. Zibordi, P. K. Quinn, J. Sciare, S. Kinne, M. Harvey, T. J. Smyth, S. Piketh, T. Zielinski, A. Proshutinsky, J. I. Goes, N. B. Nelson, P. Larouche, V. F. Radionov, P. Goloub, K. Krishna Moorthy, R. Matarrese, E. J. Robertson, and F. Jourdin (2009), Maritime Aerosol Network as a component of Aerosol Robotic Network, *Journal of Geophysical Research: Atmospheres, 114*(D06204), doi:10.1029/2008JD011257.

Tegen, I., S. P. Harrison, K. Kohfeld, I. C. Prentice, M. Coe, and M. Heimann (2002), Impact of vegetation and preferential source areas on global dust aerosol: Results from a model study., *Journal of Geophysical Research, 107(D21)*, 4576, doi:10.1029/2001JD000963.

Tesche, M., A. Ansmann, D. Müller, D. Althausen, I. Mattis, B. Heese, V. Freudenthaler, M. Wiegner, M. Esselborn, G. Pisani, and P. Knippertz (2009a), Vertical profiling of Saharan dust with Raman lidars and airborne HSRL in southern Morocco during SAMUM, *Tellus Series B, 61*, 144–164.

Tesche, M., A. Ansmann, D. Müller, R. Althausen, D. Engelmann, V. Freudenthaler, and S. Groß (2009b), Vertically resolved separation of dust and smoke over Cape Verde using multiwavelength Raman and polarization lidars during Saharan Mineral Dust Experiment 2008, *Journal of Geophysical Research*, *114*, D13202, doi:10.1029/2009JD011862.

Tesche, M., S. Groß, A. Ansmann, D. Müller, D. Althausen, V. Freudenthaler, and M. Esselborn (2011), Profiling of Saharan dust and biomass-burning smoke with multiwavelength polarization Raman lidar at Cape Verde, *Tellus Series B*, *63*, 649–676, doi: 10.1111/j.1600-0889.2011.00548.x.

Usher, C. R., A. E. Michel, and V. H. Grassian (2003), Reactions on mineral dust, *Chem. Rev.*, *103*, 4883–4939.

van Leer, B. (1977), Towards the ultimate conservative difference scheme. IV. A new approach to numerical convection, *J. Comput. Phys.*, *32*, 101–136.

Wandinger, U. (2005), Introduction to lidar, in *Lidar: Range–Resolved Optical Remote Sensing of the Atmosphere*, edited by C. Weitkamp, pp. 1–18, Springer.

Wandinger, U., D. Müller, C. Böckmann, D. Althausen, V. Matthias, J. Bösenberg, V. Weiß, M. Fiebig, M. Wendisch, A. Stohl, and A. Ansmann (2002), Optical and microphysical characterization of biomass- burning and industrial-pollution aerosols from- multiwavelength lidar and aircraft measurements, *Journal of Geophysical Research: Atmospheres*, *107*(D21), LAC 7-1–LAC 7-20, doi:10.1029/2000JD000202, 8125.

Weinzierl, B., A. Petzold, M. Esselborn, M. Wirth, K. Rasp, K. Kandler, L. Schütz, P. Koepke, and M. Fiebig (2009), Airborne measurements of dust layer properties, particle size distribution and mixing state of Saharan dust during SAMUM 2006, *Tellus Series B*, *61*(1), 96–117, doi:10.1111/j.1600-0889.2008.00392.x.

White, B. R. (1979), soil transport by winds on Mars, *Journal of Geophysical Research: Solid Earth*, *84*(B9), 4643–4651, doi:10.1029/JB084iB09p04643.

Zhang, L., J. P. Gong, and L. Barrie (2001), A size-segregated particle dry deposition scheme for an atmospheric aerosol module, *Atmos. Environ.*, *35*, 549–560.

List of Abbreviations

Abbreviation	Description
a.u.	arbitrary unit
AERONET	Aerosol Robotic Network
AOD, AOT	Aerosol Optical Depth, Aerosol Optical Thickness
asl	above sea level
BSC	Barcelona Supercomputing Center
CAM	Camera
CCN	Cloud Condensation Nuclei
CNS	Centro Nacional de Supercomputación
DAQ	Data Acquisition
DREAM	Dust Regional Atmospheric Model
DWD	*Deutscher Wetterdienst* (german for 'German Weather Service')
ECMWF	European Centre for Medium–range Weather Forecasts
EARLINET	European Aerosol Research Lidar Network
e.g.	for example
Eq.	Equation
EU	European Union
FAO	Food and Agriculture Organization of the United Nations
Fig.	Figure
FT	Free Troposphere
GDAS	Global Data Assimilation System
GEMS	Global and regional Earth-system Monitoring using Satellite and in-situ data
et al.	*et alii* (latin for 'and others')
HATPRO	Humidity And Temperature Profiler
HYSPLIT	Hybrid Single–Particle Lagrangian Integrated Trajectory model
ICoD	Euro-Mediterranean Center on Insular Cloud Dynamics
i.e.	*id est* (latin for 'it is')
IL	Intermediate Layer
IN	Ice Nuclei

IPCC	International Panel on Climate Change
IRI	International Research Institute for Climate and Society
ITCZ	Inter–Tropical Convergence Zone
Laser	Light amplification by stimulated emission of radiation
Lidar	Light detection and ranging
LT	Local Time
LWP	Liquid–Water Path
MACC	Monitoring Atmospheric Composition & Climate
MAN	Maritime Aerosol Network
MBL	Marine Boundary Layer
MODIS	Moderate Resolution Imaging Spectroradiometer
NASA	National Aeronautics and Space Administration
NCEP	National Centers for Environmental Prediction
Nd:YAG	Neodymium–doped yttrium aluminum garnet
NMMB	Nonhydrostatic Multiscale Model on the B–grid
N/R	Near–range
NOAA	National Oceanic and Atmospheric Administration
OCEANET	OCEANET project
PM	Particulate Matter
PMT	Photomultiplier Tubes
POLIPHON	Polarization–Lidar Photometer Networking
Polly^{XT}	(Portable Lidar System Extended)
PROMOTE	PROMOTE project
RRTM	Rapid Radiative Transfer Model
RV	Research Vessel
RFOV	Receiver Field of View
SAL	Saharan Air Layer
SALTRACE	Saharan Aerosol Long-range Transport and Aerosol-Cloud-Interaction Experiment
SAMUM	Saharan Mineral Dust Experiment
SCL	Sub Cloud Layer
Sect.	Section
STATSGO	State Soil Geographic Data Base
TC	Tropical Cyclones
TROPOS	*Leibniz–Institut für Troposphärenforschung Leipzig* (german for 'Leibniz Institute for Tropospheric Research Leipzig')
UTC	Universal Time Coordinated (also GMT, Greenwich Mean Time)
UV	Ultraviolet

List of Figures

List of Tables

Acknowledgements

Statement of Authenticity

I hereby certify that this master thesis has been composed by myself and contains no copy or paraphrase of material previously published or written by another person unless otherwise acknowledged in the text. All references and verbatim extracts have been quoted, and all sources of information have been specifically acknowledged. It has not been accepted in any previous application for the award of any other degree in any tertiary institution.

Upon positive assessment of this thesis, I agree that copies of my presented thesis may remain at the disposal of the libraries of the Faculty of Physics and Earth Sciences, University of Leipzig, and the Leibniz Institute for Tropospheric Research, Leipzig.

Leipzig, July 22, 2015   ....

                                          Franziska Rittmeister